The Astronomical Journal, 160:113 (18pp), 2020 September https://doi.org/10.3847/1538-3881/aba0b5

HD 191939: Three Sub-Neptunes Transiting a Sun-like Star Only 54 pc Away

Mariona Badenas-Agusti[1,2], Maximilian N. Günther[2,29], Tansu Daylan[2,30], Thomas Mikal-Evans[2], Andrew Vanderburg[3,31], Chelsea X. Huang[2,29], Elisabeth Matthews[2], Benjamin V. Rackham[2,4,32], Allyson Bieryla[5], Keivan G. Stassun[6,7], Stephen R. Kane[8], Avi Shporer[2], Benjamin J. Fulton[9,10], Michelle L. Hill[8], Grzegorz Nowak[11,12], Ignasi Ribas[13,14], Enric Pallé[11,12], Jon M. Jenkins[15], David W. Latham[5], Sara Seager[1,2,16], George R. Ricker[2], Roland K. Vanderspek[2], Joshua N. Winn[17], Oriol Abril-Pla[18], Karen A. Collins[5], Pere Guerra Serra[19], Prajwal Niraula[1], Zafar Rustamkulov[20], Thomas Barclay[21,22], Ian J. M. Crossfield[2,23], Steve B. Howell[15], David R. Ciardi[24], Erica J. Gonzales[25,33], Joshua E. Schlieder[21], Douglas A. Caldwell[26], Michael Fausnaugh[2], Scott McDermott[27], Martin Paegert[5], Joshua Pepper[28], Mark E. Rose[15], and Joseph D. Twicken[26]

[1] Department of Earth, Atmospheric and Planetary Sciences, Massachusetts Institute of Technology, Cambridge, MA 02139, USA; mbadenas@mit.edu
[2] Department of Physics and Kavli Institute for Astrophysics and Space Research, Massachusetts Institute of Technology, Cambridge, MA 02139, USA
[3] Department of Astronomy, The University of Texas at Austin, Austin, TX 78712, USA
[4] Department of Earth and Planetary Sciences, MIT, 77 Massachusetts Avenue, Cambridge, MA 02139, USA
[5] Harvard-Smithsonian | Center for Astrophysics, 60 Garden Street, Cambridge, MA 02138, USA
[6] Department of Physics and Astronomy, Vanderbilt University, 6301 Stevenson Center Lane, Nashville, TN 37235, USA
[7] Department of Physics, Fisk University, 1000 17th Avenue N, Nashville, TN 37208, USA
[8] Department of Earth and Planetary Sciences, University of California, Riverside, CA 92521, USA
[9] California Institute of Technology, Pasadena, CA 91125, USA
[10] IPAC-NASA Exoplanet Science Institute Pasadena, CA 91125, USA
[11] Instituto de Astrofísica de Canarias (IAC), E-38200 La Laguna, Tenerife, Spain
[12] Departamento de Astrofísica, Universidad de La Laguna, E-38206 La Laguna, Tenerife, Spain
[13] Institut de Ciències de l'Espai (ICE, CSIC), Campus UAB, C/Can Magrans, s/n, E-08193 Bellaterra, Spain
[14] Institut d'Estudis Espacials de Catalunya (IEEC), E-08034 Barcelona, Spain
[15] NASA Ames Research Center, Moffett Field, CA, 94035, USA
[16] Department of Aeronautics and Astronautics, Massachusetts Institute of Technology, Cambridge, MA 02139, USA
[17] Department of Astrophysical Sciences, Princeton University, 4 Ivy Lane, Princeton, NJ 08544, USA
[18] Statistics Division, Universitat Pompeu Fabra, Ramon Trias Fargas 25-27, E-08005 Barcelona, Spain
[19] Observatori Astronòmic Albanyà, Camí de Bassegoda s/n, E-17733, Albanyà, Spain
[20] Department of Earth and Planetary Sciences, Johns Hopkins University, Baltimore, MD, USA
[21] NASA Goddard Space Flight Center, Greenbelt, MD 20771, USA
[22] University of Maryland, Baltimore County, 1000 Hilltop Circle, Baltimore, MD 21250, USA
[23] Department of Physics and Astronomy, The University of Kansas, 1251 Wescoe Hall Drive, Lawrence, KS 66045, USA
[24] Caltech/IPAC, 1200 East California Boulevard, Pasadena, CA 91125, USA
[25] Department of Astronomy and Astrophysics, University of California Santa Cruz, 1156 High Street, Santa Cruz, CA 95060, USA
[26] SETI Institute/NASA Ames Research Center, Moffett Field, CA 94035, USA
[27] Proto-Logic LLC, 1718 Euclid Street NW, Washington, DC 20009, USA
[28] Department of Physics, Lehigh University, 16 Memorial Drive East, Bethlehem, PA 18015, USA
Received 2020 February 10; revised 2020 June 19; accepted 2020 June 25; published 2020 August 14

Abstract

We present the discovery of three sub-Neptune-sized planets transiting the nearby and bright Sun-like star HD 191939 (TIC 269701147, TOI 1339), a $K_s = 7.18$ mag G8 V dwarf at a distance of only 54 pc. We validate the planetary nature of the transit signals by combining 5 months of data from the Transiting Exoplanet Survey Satellite with follow-up ground-based photometry, archival optical images, radial velocities, and high angular resolution observations. The three sub-Neptunes have similar radii ($R_b = 3.42^{+0.11}_{-0.11}$, $R_c = 3.23^{+0.11}_{-0.11}$, and $R_d = 3.16^{+0.11}_{-0.11}\,R_\oplus$), and their orbits are consistent with a stable, circular, and coplanar architecture near mean-motion resonances of 1:3 and 3:4 ($P_b = 8.88$, $P_c = 28.58$, and $P_d = 38.35$ days). The HD 191939 system is an excellent candidate for precise mass determinations of the planets with high-resolution spectroscopy due to the host star's brightness and low chromospheric activity. Moreover, the system's compact and near-resonant nature can provide an independent way to measure planetary masses via transit timing variations while also enabling dynamical and evolutionary studies. Finally, as a promising target for multiwavelength transmission spectroscopy of all three planets' atmospheres, HD 191939 can offer valuable insight into multiple sub-Neptunes born from a protoplanetary disk that may have resembled that of the early Sun.

Unified Astronomy Thesaurus concepts: Exoplanet systems (484); Exoplanets (498); Transit photometry (1709); Exoplanet detection methods (489); Astronomical techniques (1684)

1. Introduction

The Transiting Exoplanet Survey Satellite (TESS; Ricker et al. 2014) was designed to detect transiting super-Earths ($R_p = 1.25$–$2\,R_\oplus$, $M_p \approx 1$–$10\,M_\oplus$) and sub-Neptunes ($R_p = 2$–$4\,R_\oplus$, $M_p \approx 10$–$40\,M_\oplus$) around the nearest and brightest

[29] Juan Carlos Torres Fellow.
[30] Kavli Fellow.
[31] NASA Sagan Fellow.
[32] 51 Pegasi b Fellow.
[33] NSF Graduate Research Fellowship Program Fellow.

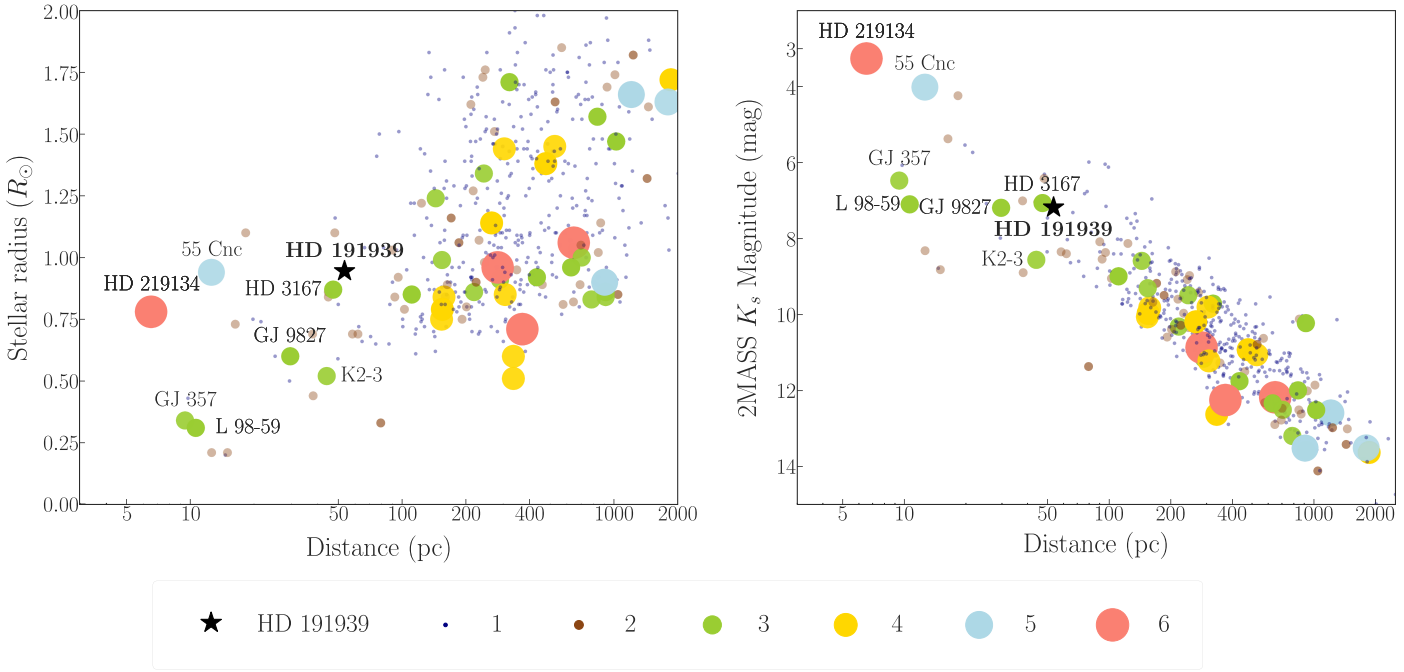

Figure 1. Host star radius and K_s magnitude of confirmed single- and multiplanet systems. In these views, we only show systems with measured masses and a relative error in planet mass, planet radius, and host star radius less than 30%. Names are only displayed for stars with at least three planets and distances less than 100 pc. The size and color of each system depends on the number of planets it hosts. Data were retrieved from the NASA Exoplanet Archive in 2020 May.

main-sequence stars. As a result, planets detected by TESS will be some of the best candidates for follow-up spectroscopy and future atmospheric characterization studies.

Since the beginning of science operations in 2018, TESS has discovered about a dozen multitransiting planet systems (e.g., Huang et al. 2018; Dragomir et al. 2019; Günther et al. 2019; Quinn et al. 2019), including some of the brightest known to date, thus yielding prime targets for detailed characterization (e.g., Huang et al. 2018; Dragomir et al. 2019; Günther et al. 2019; Quinn et al. 2019). These "multis" are excellent laboratories to perform comparative exoplanetology and learn about planetary formation and evolutionary processes in the controlled environment of the host star. Moreover, they often have a greater scientific potential than single-planet systems because they can be characterized comprehensively beyond the conventional methods of transit photometry and radial velocity (RV) observations (Ragozzine & Holman 2010). For example, measurements of transit timing variations (TTVs) can help constrain planetary masses and orbital architectures (Miralda-Escudé 2002; Agol et al. 2005). For multis amenable to atmospheric characterization, transmission spectroscopy can shed light on the shared properties of planets born from the same protoplanetary disk.

The Kepler mission revealed that multitransiting planet systems are ubiquitous (Latham et al. 2011; Lissauer et al. 2011, 2014; Rowe et al. 2014), particularly in the super-Earth to mini-Neptune regime (e.g., Howard et al. 2010; Fressin et al. 2013). Despite their widespread occurrence, the majority of Kepler multis are too faint, distant, and/or small to precisely determine planetary masses with independent (RV) surveys. Consequently, many of them lack mass and density measurements. With TESS, however, the population of multis amenable to follow-up studies will grow as nearer and brighter systems are detected. Many of these TESS discoveries will be sub-Jovian-sized planets well suited for spectroscopic studies of planetary masses (e.g., Cloutier et al. 2018) and atmospheres (e.g., Kempton et al. 2018) due to their larger sizes and their host star's proximity and brightness.

Here we focus on HD 191939 (TOI 1339, TIC 269701147), a bright ($V = 8.97$, $K = 7.18$ mag), nearby ($d = 53.48^{+0.19}_{-0.20}$ pc), Sun-like (G8 V) star with a radius of $R_* = 0.945 \pm 0.021\,R_\odot$, a mass of $M_* = 0.92 \pm 0.06\,M_\odot$, and a temperature of $T_{\rm eff} = 5400 \pm 50$ K. Using TESS data from sectors 15–19, we present the discovery of three sub-Neptune-sized planets around HD 191939 and validate their transit signals with archival optical images, RVs, ground-based photometric follow-up, and high-resolution imaging. At a distance of only 54 pc, HD 191939 is one of the nearest and brightest multitransiting planet systems known to date (see Figure 1). Due to the host star's proximity, brightness, and low chromospheric activity, this multi is an excellent target for follow-up photometric and spectroscopic studies. As we step into the era of the James Webb Space Telescope (JWST), HD 191939 is a promising candidate for detailed atmospheric characterization as well.

This paper is organized as follows. Section 2 presents the TESS photometry and the available optical, photometric, and spectroscopic observations of HD 191939. In Section 3, we constrain the stellar parameters of HD 191939. Section 4 examines multiple false-positive scenarios and confirms the planetary nature of the TESS transit signals. In Section 5, we describe our transit fitting routine, determine the system's physical and orbital parameters, investigate its dynamical properties, and discuss its prospects for atmospheric characterization. Section 6 places HD 191939 in the context of known planetary systems and highlights possible research avenues to improve our current knowledge of it. Finally, we summarize our results and present our conclusions in Section 7.

Table 1
Stellar Properties of HD 191939

Property	Value	Source
Other Target Names		
HD ID	191939	4
TOI ID	1339	...
TIC ID	269701147	1
2MASS ID	J20080574+6651019	2
Gaia DR2 ID	2248126315275354496	3
Astrometric Properties		
R.A. (J2015.5; h:m:s)	20:08:06.150	3
Decl. (J2015.5; d:m:s)	+66:51:01.08	3
Parallax (mas)	18.706 ± 0.071	7
$\mu_{\rm R.A.}$ (mas y^{-1})	150.256 ± 0.044	3
$\mu_{\rm Decl.}$ (mas y^{-1})	−63.909 ± 0.047	3
Photometric Properties		
TESS (mag)	8.292 ± 0.006	1
B (mag)	9.720 ± 0.038	5
V (mag)	8.97 ± 0.03	6
Gaia (mag)	8.7748 ± 0.0002	3
J (mag)	7.597 ± 0.029	2
H (mag)	7.215 ± 0.023	2
K_s (mag)	7.180 ± 0.021	2

References. (1) TESS Input Catalog Version 8 (TICv8; Stassun et al. 2018), (2) 2MASS (Cutri et al. 2003), (3) Gaia DR2 (Brown et al. 2018), (4) Henry Draper Catalog (Cannon & Pickering 1993), (5) Tycho2 Catalog (Høg et al. 2000), (6) Hipparcos Catalog (van Leeuwen 2007), (7) Gaia DR2 parallax and uncertainty from TICv8, corrected for a systematic offset of +0.082 ± 0.033 mas, as described in Stassun & Torres (2018).

2. Observations

2.1. TESS Photometry

With a TESS magnitude of $T = 8.29$ mag, a radius smaller than the Sun's ($R_* = 0.945 \pm 0.021\,R_\oplus$), and a low contaminating ratio (∼0.005), HD 191939 was included in the TESS Candidate Target List as a high-priority target (Stassun et al. 2018). As such, HD 191939 was preselected for 2 minutes. Observations consisting of 11 × 11 pixel subarrays centered on the target. The star's astrometric and photometric properties are listed in Table 1.

The TESS spacecraft observed HD 191939 (R.A. J2015.5 = 20:08:06.150, decl. J2015.5 = +66:51:01.08) during sectors 14–19 (2019 July 18 to 2019 December 24). After visually inspecting the target pixel files, we found that the host star had fallen outside of the CCD's science image area in sector 14. We thus performed our analysis with data from sectors 15–19.

The photometric observations for HD 191939 (see Figure 2) were processed through the Science Processing Operations Center (SPOC) pipeline, developed and maintained by the NASA Ames Research Center (Jenkins et al. 2016; Jenkins 2017).[34] The pipeline detected two tentative planetary signals in the combined transit search for sectors 15 and 16. With the addition of sectors 17–19, the MIT Quick-Look Pipeline (QLP; C. X. Huang et al. 2020, in preparation) identified three recurring transit signals.

The phase-folded light curves obtained with the SPOC transit parameters had a flat-bottomed shape consistent with a planetary interpretation of the transits. Moreover, the two planet candidates passed all of the SPOC and QLP standard validation diagnostics, including a search for secondary eclipses, differences in odd and even transits, and flux centroid offsets during transit (see Section 4.1).

We retrieved the SPOC-processed data from the Mikulski Archive for Space Telescopes (MAST).[35] In particular, we downloaded the Presearch Data Conditioning (PDC) light curves and removed all observations encoded as *NaN* or flagged as bad-quality points by the SPOC pipeline. From a total of 85,282 photometric measurements (17,848, 16,812, 16,945, 16,612, and 17,065 for sectors 15–19, respectively), we identified a total of 4980 bad-quality data points, which we excluded from further analysis.

2.2. Ground-based Photometry: Observatori Astronòmic Albanyà

As part of the TFOP follow-up program,[36] we acquired 320 photometric exposures of HD 191939 on 2019 October 29 with the 0.4 m telescope at the Observatori Astronòmic Albanyà (OAA) in Catalonia (Spain). The host star was continuously observed for 398.8 minutes in the Cousins I_c filter using a CCD camera with a resolution of 3056 × 3056 pixels and a pixel scale of 0.″72 pixel^{-1}. The science exposures were reduced with the AstroImageJ (AIJ) software (Collins et al. 2017).

2.3. Archival Spectroscopic Observations: SOPHIE

SOPHIE (Perruchot et al. 2008; Bouchy et al. 2009) is a fiber-fed echelle spectrograph mounted on the 1.93 m telescope at the Observatoire de Haute-Provence (OHP) in France. This instrument observed HD 191939 between 2007 September 27 and 2007 November 30 with an RV precision of 4–5 m s^{-1} (e.g., Bouchy et al. 2009, 2011). A total of five spectra were acquired with SOPHIE's high-resolution mode, which provides a resolving power of $\lambda/\Delta\lambda \equiv R = 75{,}000$. The spectra have a median exposure time of 617 s and a median signal-to-noise ratio (S/N) per pixel at 550 nm of 59 (see Table 2).

We downloaded all available observations of HD 191939 from the SOPHIE public archive (Moultaka et al. 2004). These included spectra reduced by the Data Reduction Software (DRS) v0.50,[37] as well as the cross-correlation functions (CCFs) determined by the DRS using a numerical mask for the G2 spectral type (Baranne et al. 1996). The CCFs were calculated over a ±30 km s^{-1} velocity interval. The RV, FWHM, and contrast of each CCF were computed by the DRS by fitting a Gaussian function to the CCF profile. We extracted barycentric-corrected RVs, FWHMs, and the bisector spans from the FITS headers of the CCFs (Coroller & Bouchy 2017). We found no correlations between either the RV measurements and the bisectors ($r = 0.51$, while the critical value of the Pearson correlation coefficient at the confidence level of 0.01 is $r_{3,0.01} = 0.96$) or the RVs and the FWHMs of the CCFs ($r = 0.43$). Such correlations would have indicated astrophysical false positives, such as stellar spots or blends.

[34] The SPOC pipeline searches for planetary transits by fitting an averaged Mandel & Agol (2002) model to the light curve with nonlinear limb-darkening coefficients as parameterized by Claret & Bloemen (2011).

[35] https://mast.stsci.edu/portal/Mashup/Clients/Mast/Portal.html
[36] https://tess.mit.edu/followup/
[37] http://www.obs-hp.fr/guide/sophie/data_products.shtml

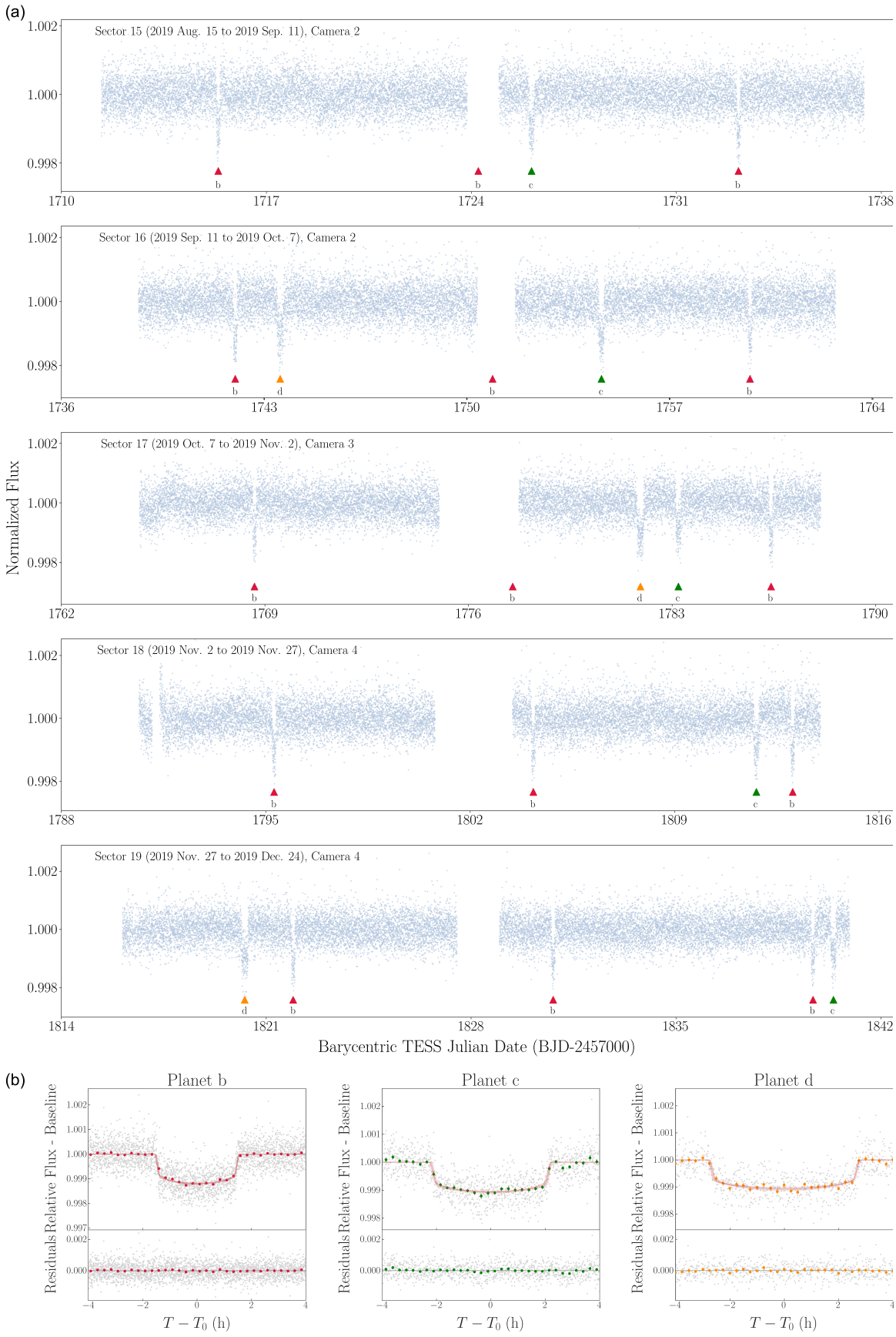

Figure 2. (a): full TESS discovery light curve based on the 2 minute exposures from sectors 15–19. The transits of planets b, c, and d are shown in red, green, and orange, respectively. (b): TESS phase-folded light curves over the `allesfitter` best-fit periods and initial epochs (see Section 5). The gray points are the TESS 2 minute exposures, the colored circles are the data points binned over 15 minutes, and the red lines represent 20 posterior models drawn from the outcome of the final fit. The light-curve residuals are shown in the bottom.

Table 2
SOPHIE RV Measurements with Their S/N at 555 nm and Their Exposure Times

BJD_{UTC} −2,450,000	RV (km s^{-1})	Error (km s^{-1})	S/N –	Exp. Time (s)
4,371.345	−9.237	0.002	42.9	600
4,372.288	−9.249	0.001	60.5	500
4,430.266	−9.213	0.001	70.8	900
4,431.296	−9.218	0.001	67.4	743
4,435.308	−9.232	0.001	54.4	346

2.4. Spectroscopic Follow-up

2.4.1. TRES Reconnaissance Spectroscopy

We obtained three spectra of HD 191939 between 2019 October 24 and 2019 November 5 using the fiber-fed Tillinghast Reflector Echelle Spectrograph (TRES; Fürész 2008) on the 1.5 m telescope at the Fred Lawrence Whipple Observatory (Mt. Hopkins, Arizona). TRES covers the spectral range 3850–9100 Å and has a resolving power of $R = 44{,}000$. The TRES spectra have an average S/N per resolution element of 47 and were extracted as described in Buchhave et al. (2010).

2.4.2. LCO/NRES Reconnaissance Spectroscopy

We acquired three consecutive 20 minute optical exposures of HD 191939 on 2019 November 1 with the Network of Echelle Spectrographs (NRES; Siverd et al. 2016, 2018), operated by Las Cumbres Observatory (LCO; Brown et al. 2013). The NRES is composed of four high-precision fiber-fed spectrographs with a resolving power of $R = 53{,}000$. The NRES spectra were stacked to remove cosmic rays and instrumental effects, resulting in a final S/N of 60.

2.5. Gemini/NIRI High Angular Resolution Imaging

We observed HD 191939 on 2019 November 8 with the Near InfraRed Imager (NIRI) at the Gemini North telescope (Hodapp et al. 2003). A total of nine adaptive optics (AO) images were collected in the Brγ filter, each with an exposure time of 2 s. The telescope was dithered in a grid pattern between each science exposure to construct the sky background frame and remove artifacts such as bad pixels and cosmic rays. Data were processed using a custom set of IDL codes with which we interpolated bad pixels, subtracted the sky background, flat-corrected images, aligned the stellar position between frames, and coadded data. We determined the sensitivity to stellar companions by injecting artificial point-spread functions into the data at a range of separation and angles and scaling these until they could be detected at 5σ. We are sensitive to stellar neighbors 5 mag (8.4 mag) fainter than HD 191939 at 200 mas (1″). Our sensitivity as a function of radius is shown in Figure 3 with a thumbnail image of HD 191939.

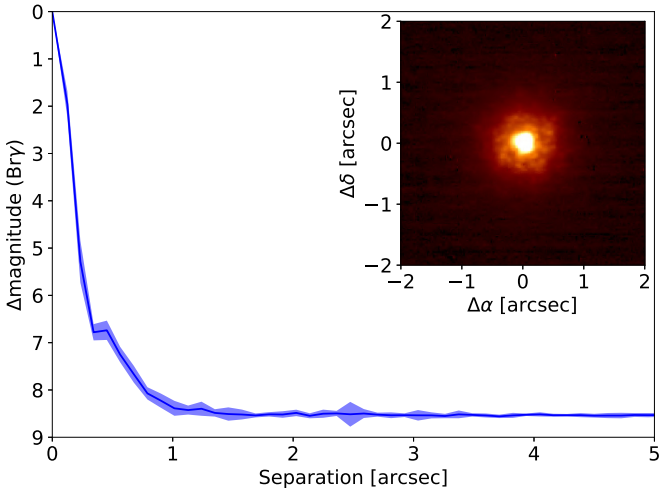

Figure 3. Sensitivity curve of our Gemini/NIRI AO images (solid blue line). We are sensitive to companions with a contrast of 5 mag just 200 mas from the star. No visual sources are seen anywhere in the field of view. A thumbnail image of the target is inset.

3. Host Star Characterization

3.1. TRES Spectroscopy

We used the TRES spectra to measure the host star's effective temperature $T_{\rm eff}$, surface gravity $\log g$, metallicity [m/H], and rotational velocity $v \sin i$ with the Stellar Parameter Classification (SPC; Buchhave et al. 2012) tool. The SPC software cross-correlates an observed spectrum against a grid of synthetic spectra based on the Kurucz atmospheric models (Kurucz 1992). The weighted average results are $T_{\rm eff} = 5427 \pm 50$ K, $\log g = 4.44 \pm 0.10$ cgs, [m/H] $= -0.16 \pm 0.08$ dex, and $v \sin i = 0.6 \pm 0.5$ km s^{-1} (see Table 3). From the TRES spectra, we also detected weak Hα absorption, indicating that HD 191939 has low stellar activity.

3.2. NRES Spectroscopy

We also constrained the stellar parameters from the NRES observations following the techniques presented in Petigura et al. (2017) and Fulton & Petigura (2018). In particular, we used the `SpecMatch` software (Petigura 2005; Petigura et al. 2017)[38] to compare the observed spectrum of HD 191939 against synthetic spectra created by linearly interpolating the Coelho et al. (2005) grid of model spectra at arbitrary sets of $T_{\rm eff}$, $\log g$, [Fe/H], and $v \sin i$. We maximized the χ^2-based likelihood via a Levenberg–Marquardt algorithm (Press et al. 1992) and found $T_{\rm eff} = 5335 \pm 100$ K, $\log g = 4.2 \pm 0.1$ cgs, [Fe/H] $= -0.13 \pm 0.06$ dex, and $v \sin i < 2$ km s^{-1}.

3.3. Spectral Energy Distribution Analysis

We used the host star's broadband spectral energy distribution (SED) and Gaia DR2 parallax to determine an empirical measurement of the stellar radius following procedures described in the literature (Stassun & Torres 2016; Stassun et al. 2017, 2018). For this analysis, we retrieved the far- and near-UV fluxes from the Galaxy Evolution Explorer; the B_T and V_T magnitudes from Tycho-2; the J, H, and K_s magnitudes from the Two Micron All Sky Survey (2MASS); the W1–W4 magnitudes from the Wide-field Infrared Survey Explorer; and the G, $G_{\rm BP}$, and $G_{\rm RP}$ magnitudes from Gaia. When taken in combination, the available photometry spans the full stellar SED over the wavelength range 0.15–22 μm (see Figure 4).

We performed a fit to the host star's SED with the Kurucz stellar atmospheric models, placing priors on $T_{\rm eff}$, $\log g$, and [m/H] based on the SPC analysis of the TRES spectra. The remaining free parameter was the extinction (A_V), which we

[38] https://github.com/petigura/specmatch-syn

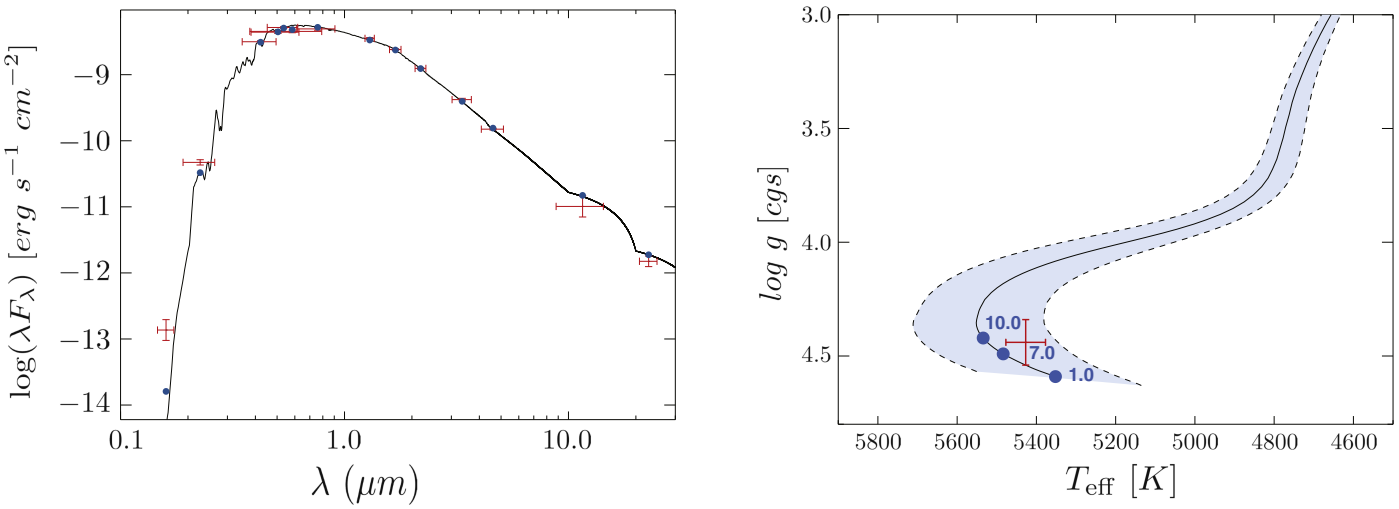

Figure 4. Left: SED. Red symbols are the observed photometric data, with the horizontal bars reflecting the effective width of the passband. Blue symbols are the model fluxes from the best-fit Kurucz atmosphere model (black). Right: H-R diagram. The black curve with blue shading represents a Yonsei–Yale evolutionary model for the stellar mass and metallicity with their uncertainties. The blue dots label ages along the evolutionary track in Gyr. The red symbol represents the spectroscopically derived effective temperature and surface gravity with their uncertainties.

Table 3
Derived Stellar Properties for HD 191939

Property	Value	Source	Reference Spectra
R_* ($R_\odot$)	0.945 ± 0.021	SED	TRES
M_* ($M_\odot$)	0.92 ± 0.06	SED via Torres et al. (2010)	TRES
Age (Gyr)	7 ± 3	SED	TRES
A_v	0.03 ± 0.03	SED	TRES
$F_{\rm bol}$ (erg s^{-1} cm^{-2})	$(7.81 \pm 0.18) \times 10^{-9}$	SED	TRES
$T_{\rm eff}$ (K)	5427 ± 50	SPC	TRES
log g (cgs)	4.40 ± 0.10	SPC	TRES
[m/H] (dex)	-0.16 ± 0.08	SPC	TRES
$(v \sin i)_{\rm A}$ (km s^{-1})	0.6 ± 0.5	SPC	TRES
L_* ($L_\odot$)	0.69 ± 0.01	`isochrones` (MIST)	TRES
Distance (pc)	$53.48^{+0.19}_{-0.20}$	`isochrones` (MIST)	TRES
ρ (g cm^{-3})	1.55 ± 0.19	`allesfitter`	
Spectral type	G8 V	Pecaut et al. (2012), Pecaut & Mamajek (2013)	
$W_{\rm H\alpha}$ (Å)	1.259 ± 0.007	This work	SOPHIE

limited to the maximum line-of-sight value from the dust maps of Schlegel et al. (1998). The model fits the data well, with a reduced χ^2 of 1.9 and best-fit extinction of $A_V = 0.03 \pm 0.03$ (see Figure 4). We also integrated the model SED to obtain a bolometric flux at Earth of $F_{\rm bol} = (7.81 \pm 0.18) \times 10^{-9}$ erg s^{-1} cm^{-2}. Using $F_{\rm bol}$, $T_{\rm eff}$, and the Gaia DR2 parallax adjusted by +0.08 mas to account for the systematic offset reported by Stassun & Torres (2018), we determined a stellar radius of $R_* = 0.945 \pm 0.021\,R_\odot$. We also estimated the stellar mass empirically. The eclipsing binary-based relations of Torres et al. (2010) yield $M_\star = 0.92 \pm 0.06\,M_\odot$, whereas the stellar surface gravity and SED-based radius result in $M_\star = 0.90 \pm 0.21\,M_\odot$. Figure 4 shows the former in a Hertzsprung–Russell (H-R) diagram with an evolutionary track from the Yonsei–Yale models (Yi et al. 2001; Spada et al. 2013). These plots imply that the age of HD 191939 is 7 ± 3 Gyr.

Finally, we used the spectroscopic $v \sin i$ and the SED-based radius to calculate a stellar rotation period of $P_{\rm rot}/\sin i = 79 \pm 66$ days, where the large uncertainty is driven by the large error on the spectroscopic $v \sin i$. This is consistent with the dominant periodicity in the TESS data (after masking the transits of the three planets) identified via a Lomb–Scargle periodogram analysis (Lomb 1976; Scargle 1982): a 44 ppm peak-to-peak roughly sinusoidal variation with a 14.15 day period and false-alarm probability of 10^{-20}.

3.4. Independent Validation of Stellar Parameters

As an independent validation on the SPC/SED stellar parameters, we used the spectroscopic properties of HD 191939 derived from the TRES and NRES spectra to perform isochrone fitting with two stellar evolutionary models: the MESA Isochrones and Stellar Tracks database (MIST; Choi et al. 2016; Dotter 2016), as implemented by the `isochrones` (Morton 2015) and `isoclassify` (Huber et al. 2017) packages, and the Padova models (da Silva et al. 2006), accessible via the `PARSEC v1.3` (Bressan et al. 2012) online tool.[39]

We ran `isochrones` and `isoclassify` with priors on the star's photometric magnitudes, the corrected Gaia DR2 parallax, and the best-fit spectroscopic parameters from either the TRES

[39] http://stev.oapd.inaf.it/cgi-bin/param_1.3

($T_{\rm eff}$, $\log g$, [m/H]) or NRES ($T_{\rm eff}$, $\log g$, [Fe/H]) spectra.[40] To implement `isoclassify`, we also accounted for extinction by incorporating the 3D dust map of Green et al. (2018), which covers most of the sky with a decl. larger than $-30°$. The derived stellar parameters are consistent with the values presented in Table 3, regardless of the choice of reference spectra for the host star's spectroscopic parameters. To assess whether this consistency was primarily due to the use of the MIST database, we also determined the stellar parameters with the Padova models with the `PARAM` v1.3 tool. For both the TRES and NRES spectroscopic parameters, the resulting stellar properties agree with the `isochrones` and `isoclassify` predictions to within 1σ. In the rest of this paper, we adopt the results from Table 3 for our analysis of the HD 191939 system.

3.5. Chromospheric Activity Indicators

The SOPHIE spectra detailed in Section 2.3 indicate that HD 191939 is chromospherically inactive. As with the TRES spectra, the five SOPHIE spectra show the Hα line in absorption. We measured the equivalent width of the Hα line ($W_{\rm H\alpha}$) in each spectrum using a 10 Å subsample centered on the vacuum wavelength of Hα (6562.81 Å). We fitted a Voigt profile to the line and a linear trend to the continuum via least squares using `astropy` (Price-Whelan et al. 2018). We estimated the uncertainties by bootstrapping the model fit 100 times, excluding a random 10% of the data points. The equivalent widths are consistent between the five spectra, and we measure a weighted-mean Hα equivalent width of $W_{\rm H\alpha} = 1.259 \pm 0.007$ Å. Visual inspection reveals no evidence of emission in the cores of the Ca II H and K or Hα lines. We conclude that these factors indicate a lack of measurable chromospheric activity for HD 191939.

4. Ruling Out False Positives

The Kepler mission revealed that multiple-period transit-like events are more likely to be caused by true planets than false positives (e.g., Latham et al. 2011; Lissauer et al. 2012). Despite such evidence, it is important to carefully inspect the observed transit signals to rule out false-positive scenarios, including instrument systematics and contamination from nearby stars. In this section, we aim to validate the HD 191939 planet candidates with the SPOC validation tests (Section 4.1), the TESS photometry and archival/follow-up observations of HD 191939 (Section 4.2), and the statistical validation software `vespa` (Section 4.3).

4.1. SPOC Validation Diagnostics

The two planet candidates identified by the SPOC Data Validation Pipeline (referred to as planets "b" and "c" in our analysis; see Section 5) pass all of the SPOC data validation (DV) tests (Twicken et al. 2018). We list these tests as follows.

1. An eclipsing binary discrimination test to search for weak secondary eclipses and compare the depth of odd and even transits. Planets b and c pass this diagnostic at 2σ, with no shallow secondaries around phase 0.5 and no odd/even transit depth variations.
2. An optical ghost diagnostic test designed to primarily rule out optical ghosts, scattered light, instrumental noise, and bright background eclipsing binaries (EBs; outside of the photometric aperture) as the source of the transit-like events. This test measures the correlation between a transit model light curve and flux time series derived from the photometric core and halo aperture pixels to determine whether the transit signature is more consistent with (1) a star in the photometric core or (2) distributed or other contamination outside the core. Planets b, c, and d all pass this diagnostic test within 2σ.
3. A difference image centroid offset test to determine if the location of the transit source is statistically consistent with the position of the target star. The offset distance for planet b in the combined sector 15–16 SPOC analysis was less than $1\farcs7$ (0.33σ). For planet c, the maximum offset distance was less than $5\farcs2$ (0.94σ).
4. A bootstrap test to assess the confidence level of the transit detection. Planets b and c pass this test with formal false-alarm probabilities of 1.05×10^{-135} and 1.72×10^{-63}, respectively.

These DV tests were not applied to the third planet around HD 191939 (planet "d"), as it was not detected by the SPOC pipeline in the combined transit search of TESS sectors 15 and 16. Nevertheless, we independently verified the planetary nature of all three planet candidates with the analyses described in the following sections.

4.2. Observational Constraints

4.2.1. Archival Optical Images

The TESS detectors have a larger pixel scale than the Kepler telescope (TESS: $\sim 21''$, Kepler: $4''$), so photometric contamination from nearby astrophysical sources is more likely. To investigate this false-positive scenario, we compared a TESS exposure of HD 191939 from sector 16 to archival optical images taken in 1953, 1991, and 2013 by the first Palomar Observatory Sky Survey (POSS-I; Minkowski & Abell 1963), the second POSS (POSS-II; Reid et al. 1991), and the Pan-STARRS survey (Kaiser et al. 2002, 2010), respectively (see Figure 5). Due to HD 191939's high proper motion, its present-day location appears unobscured in the archival images. Based on the POSS-I field of view, when HD 191939 was $\sim 11''$ away from its current sky position due to proper motion, we estimate that any $V \lesssim 19$ stars would have been clearly visible where HD 191939 is located today (e.g., a $V = 18.34$ source, identified as Gaia DR2 2248126310978337408, can be observed in the bottom left corner of the POSS-I view).

We performed a query of the Gaia DR2 and 2MASS catalogs centered on HD 191939 and used the SPOC reports to identify potential background sources around the host star. Within the central TESS pixel, there is only one 2MASS source at $13\farcs6$ separation with a TESS magnitude of $T = 14.70$ mag (2MASS J20080397+6651023; TIC 269701145). However, this object is likely a spurious 2MASS detection. First, 2MASS artifacts are known to appear around bright stars, typically along their diffraction spikes (Stassun et al. 2018). Second, it was only observed in the J band ($J = 14.2$ mag), not in the H and K bands (2MASS photometric quality flag of "AUU" and read flag of 0 for the H and K bands; Cutri et al. 2003). Third, it is likely that Gaia DR2 would have detected this 2MASS object, provided it were real. With a Gaia magnitude difference of $\Delta G \sim 5.4$ mag

[40] For the TRES spectra, we assumed that [m/H] was a good first-order initial guess for [Fe/H], as Sun-like stars such as HD 191939 are not particularly enriched in alpha elements.

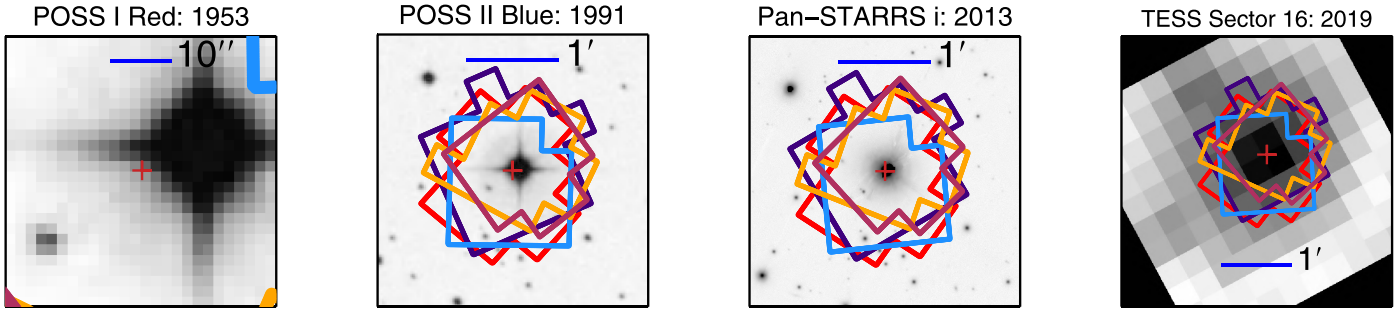

Figure 5. Archival images and TESS view of the field around HD 191939 from 1953 to 2019. North is up, and east is to the left. The red plus sign is the star's current location, and the red, purple, light blue, orange, and maroon regions are the TESS photometric apertures for sectors 15, 16, 17, 18, and 19, respectively. Due to the star's proper motion, there is an offset between its present-day position and its location in the original POSS images.

relative to HD 191939,[41] this source would have been within the observable parameter space of Gaia DR2's contrast sensitivity curve (Brandeker & Cataldi 2019). Fourth, the Pan-STARRS images for HD 191939 in the *grizy* filters (e.g., see Figure 5) do not reveal any stellar objects near the position of the 2MASS source. Given the high level of completeness of the Pan-STARRS survey down to its limiting magnitude (*grizy* $\sim$ 22.4), it is thus improbable that the 2MASS source is a true star. Finally, we can rule out the existence of this artifact with ground-based photometry (see Section 4.2.2). With all of the aforementioned evidence, we conclude that the 2MASS source is an instrumental artifact and could not have caused the transit-like events in the TESS light curve.

4.2.2. Ground-based Photometry

The OAA observations covered a full transit of the inner planet, HD 191939 b, and showed a possible detection of a roughly 1200 ppm transit within a 13″ photometric aperture. However, the data were not of sufficient quality to include in our global model fit. The longer periods of the planet candidates c and d have prevented successful ground-based photometric follow-up of their transits thus far.

To rule out nearby EBs, we conducted aperture photometry of all visible sources within 2.′5 of HD 191939 using a photometric aperture radius of 13″. For each source, we employed the AIJ software to determine the rms error of its light curve, the predicted transit depth on the target star, and the resulting S/N. None of the sources considered in this analysis are bright enough to be a potential source of the TESS detection. Moreover, the OAA exposures show no evidence of the apparent 2MASS instrumental artifact discussed in Section 4.2.1.

4.2.3. High-resolution Imaging

It is important to check for stellar companions that can dilute the light curve, thus biasing the measured planetary radius or even being the source of false positives (Ciardi et al. 2015). To search for such companions, we examined the AO Gemini/NIRI final image (see Section 2.5) and found no visible stellar objects in the field of view around HD 191939 (Figure 3).

[41] The 2MASS detection lacks optical photometry, so there is no reliable way of estimating its Gaia magnitude. To calculate ΔG, we assume that this object is very red (e.g., a late M dwarf) and take its 2MASS *J*-band magnitude as an approximation of its Gaia magnitude. This conservative approach provides an estimate of how faint the 2MASS source could be in the Gaia bandpass.

4.2.4. Archival RVs

We performed a joint fit to the SOPHIE RV and TESS observations with the `allesfitter` package (Günther & Daylan 2020)[42] to rule out possible substellar or stellar companions. Our combined fit finds a 3σ upper limit on the RV semiamplitudes (K) of $K_b < 250$, $K_c < 300$, and $K_d < 250\,\mathrm{m\,s^{-1}}$ for planet candidates b, c, and d, respectively. In contrast, a brown dwarf ($M \approx 13\,M_{\rm Jup}$) around HD 191939 would have $K_b = 620$, $K_c = 420$, and $K_d = 380\,\mathrm{m\,s^{-1}}$. The SOPHIE constraints lie well below these values, thus pointing to the planetary origin of the TESS transits.

In addition, we estimated the RV semiamplitudes of the HD 191939 planet candidates from the standard RV equation (see Equation (14) in Lovis & Fischer 2010) using the `allesfitter` orbital results (see Table 4) and the planets' masses predicted via the probabilistic mass–radius (MR) relation of Wolfgang et al. (2016, hereafter W16). To estimate the HD 191939 planetary masses, we used the full `allesfitter` posterior for the planetary radii and samples from the posterior of the parameters that define Equation (2) in W16. This yields $M_b = 14.77^{+1.98}_{-1.97}$, $M_c = 13.85^{+1.87}_{-1.85}$, and $M_d = 13.50^{+1.84}_{-1.80}\,M_\oplus$ for planet candidates b, c, and d, respectively. In turn, these masses correspond to RV semiamplitudes ($K_b = 2.0 \pm 0.6$, $K_c = 1.0 \pm 0.4$, and $K_d = 1.0 \pm 0.4\,\mathrm{m\,s^{-1}}$) well within the range of the SOPHIE predictions. We also estimated the planetary masses and RV semiamplitudes with the probabilistic MR relation of Chen & Kipping (2017) and found consistent results.

4.2.5. Ingress/Egress Test

We investigated whether a chance-aligned background or foreground EB could have caused the observed transits in the TESS light curve by placing an upper limit on the magnitude of a fully blended star. In a scenario of photometric contamination by blended light, the observed TESS transit depth ($\delta_{\rm obs}$) is given by

$$\delta_{\rm obs} \simeq \left(\frac{R_{p,\rm true}}{R_*}\right)^2 \frac{F_{\rm blend}}{F_{\rm blend} + F_{\rm star}} = \delta_{\rm true}\frac{f}{1+f}, \qquad (1)$$

where f is the flux ratio $f \equiv F_{\rm blend}/F_{\rm star}$, $\delta_{\rm true}$ is the square of the true planet-to-star radius ratio in the absence of a blend, $F_{\rm blend}$ is the flux of the contaminating source, and $F_{\rm star}$ is the flux of HD 191939. Under the assumption of a central transit (i.e., $b = 0$), the observed transit depth $\delta_{\rm obs}$ must satisfy (Equation (21)

[42] https://github.com/MNGuenther/allesfitter

Table 4
Final Model Fit Results

Parameter	HD 191939 b	HD 191939 c	HD 191939 d
Radius ratio, $R_p/R_\star$	$0.03343^{+0.00043}_{-0.00043}$	$0.03158^{+0.00054}_{-0.00054}$	$0.03089^{+0.00060}_{-0.00060}$
Sum of radii over semimajor axis, $(R_\star + R_p)/a$	$0.0553^{+0.0023}_{-0.0020}$	$0.02548^{+0.0011}_{-0.00095}$	$0.02084^{+0.00097}_{-0.00081}$
Cosine of orbital inclination, $\cos i$	$0.0317^{+0.0036}_{-0.0036}$	$0.0153^{+0.0017}_{-0.0016}$	$0.0089^{+0.0020}_{-0.0020}$
Mid-transit time, T_0 (BJD days)	$2458{,}715.355{,}54^{+0.00064}_{-0.00064}$	$2458{,}726.053{,}1^{+0.0011}_{-0.0011}$	$2458{,}743.550{,}5^{+0.0015}_{-0.0015}$
Orbital period, P (days)	$8.880403^{+0.000070}_{-0.000070}$	$28.58059^{+0.00045}_{-0.00045}$	$38.3561^{+0.0012}_{-0.0012}$
Transit depth, $\delta_{\mathrm{dil;TESS}}$ (ppt)	$1.199^{+0.023}_{-0.025}$	$1.059^{+0.030}_{-0.030}$	$1.072^{+0.038}_{-0.038}$
Planet radius, R_p ($R_\oplus$)	$3.42^{+0.11}_{-0.11}$	$3.23^{+0.11}_{-0.11}$	$3.16^{+0.11}_{-0.11}$
Semimajor axis, a (au)	$0.0814^{+0.0040}_{-0.0040}$	$0.1762^{+0.0089}_{-0.0089}$	$0.215^{+0.011}_{-0.011}$
Orbital inclination, i (deg)	$88.18^{+0.21}_{-0.21}$	$89.124^{+0.091}_{-0.097}$	$89.49^{+0.12}_{-0.12}$
Impact parameter, b_{tra}	$0.593^{+0.041}_{-0.045}$	$0.619^{+0.040}_{-0.043}$	$0.439^{+0.074}_{-0.088}$
Total transit duration, T_{tot} (hr)	$3.075^{+0.022}_{-0.022}$	$4.455^{+0.039}_{-0.039}$	$5.527^{+0.046}_{-0.046}$
Full transit duration, T_{full} (hr)	$2.772^{+0.025}_{-0.025}$	$4.018^{+0.046}_{-0.046}$	$5.116^{+0.056}_{-0.052}$
Equilibrium temperature, T_{eq} (K)	812^{+18}_{-17}	552^{+13}_{-11}	499^{+12}_{-11}
System Parameters in the TESS Bandpass			
Limb-darkening coefficient 1, $u_{1;\mathrm{TESS}}$	$0.52^{+0.15}_{-0.21}$		
Limb-darkening coefficient 2, $u_{2;\mathrm{TESS}}$	$-0.09^{+0.27}_{-0.19}$		
Flux error, $\log\sigma_{\mathrm{TESS}}$ (logrel. flux.)	$-7.6797^{+0.0028}_{-0.0028}$		
GP characteristic amplitude, gp: $\log\sigma$(TESS)	$-9.489^{+0.046}_{-0.046}$		
GP timescale, gp: $\log\rho$(TESS)	$-1.32^{+0.13}_{-0.13}$		

in Seager & Mallen-Ornelas 2003)

$$\delta_{\mathrm{obs}} \leqslant \delta_{\mathrm{blend}} = \frac{\left(1 - \frac{t_F}{t_T}\right)^2}{\left(1 + \frac{t_F}{t_T}\right)^2}, \quad (2)$$

where t_F/t_T is the ratio of the full transit duration to the total transit duration t_T, which parameterizes the transit shape.[43] For each planet candidate, we generated posterior probability distributions for the transit observables (i.e., δ_{obs}, t_T, and t_F) by fitting the TESS light curve with `allesfitter` with the transits of the other planet candidates masked out. From these posteriors, we used Equation (2) to estimate the maximum transit depth caused by the contaminating star (δ_{blend}) and determine a 3σ lower limit for t_F/t_T. For all planet candidates, we find $t_F/t_T \sim 0.90$, which suggests that the transits are box-shaped and thus less likely to be caused by a blend (Seager & Mallen-Ornelas 2003).

To determine the TESS magnitude of the faintest blended star (m_{blend}) capable of producing the observed transits in the TESS light curve, we calculated the flux ratio f with Equation (1) and exploited the relation between stellar magnitudes and fluxes ($m_{\mathrm{blend}} - m_{\mathrm{star}} = -2.5\log_{10} f$, where m_{star} is the TESS magnitude of HD 191939). Our analysis rules out blended stars fainter than 10.13, 10.38, and 9.50 at a 3σ level for planet candidates b, c, and d, respectively. Therefore, objects such as the spurious 2MASS detection mentioned in Section 4.2.1 would automatically be discarded as the cause of the observed TESS transits. Other nearby stars within the TESS photometric aperture, such as TIC 269701151 (at 42.″81 with $T = 15.63$) and TIC 269701155 (at 45.″59 with $T = 15.84$), would not be bright enough either to produce the observed transit-like events. Consequently, the results of the ingress–egress test support the planetary nature of the TESS transit signals.

[43] The full transit duration is the time between ingress and egress (i.e., second to third contact). The total transit duration is the time between first and fourth contact.

4.3. Statistical Validation of the HD 191939 System

The public software `vespa` (Morton 2012) uses Bayesian inference to calculate the probability that the TESS transits are compatible with astrophysical false-positive scenarios. For each HD 191939 planet candidate, we ran `vespa` with the planet's TESS phase-folded light curve; the `allesfitter` best-fit results for its orbital period, transit depth, and planet-to-star radius ratio (see Section 5, Table 4); and the host star's Gaia DR2 coordinates, photometric magnitudes, and effective temperature, metallicity, and surface gravity (see Table 1). We also included three observational constraints in our false-positive probability (FPP) calculation, namely, the Gemini/NIRI contrast curve (see Section 2.5), a maximum blend radius of 1″ based on the high-contrast sensitivity analysis from Section 4.2.3, and a maximum depth of a potential secondary eclipse of 5×10^{-5}. To calculate the latter, we masked out the observed transits of planet candidates b, c, and d on the full TESS discovery light curve and estimated an upper limit on the shallowest transit depth that could be detected by running a box-fitting least-squares algorithm with the public software `lightkurve` (Lightkurve Collaboration et al. 2018).

The resulting FPPs are less than 10^{-6} for all three planet candidates. Given that multiple transit-like signatures are more likely to be caused by genuine planets than false positives, these FPPs must be enhanced by a "multiplicity boost" corresponding to ∼15 for TESS targets (Guerrero 2020). For TESS planets with sizes up to $R_p = 6\,R_\oplus$, this factor increases to 60. When applying the latter to our `vespa` results, we obtain FPPs lower than 10^{-7} for all planet candidates. We thus conclude that HD 191939 has three statistically validated bona fide planets and refer to them as planets b, c, and d in our subsequent analysis.

5. Global Model Fit: Orbital and Planetary Parameters

We first employed the publicly available Transit Least Squares (TLS) package (Hippke & Heller 2019) to look for planetary transits in the TESS light curve (see Figure 2).[44] The TLS routine identified three possible planetary signals with periods of $P_b \approx 8.88$, $P_c \approx 28.58$, and $P_d \approx 38.35$ days, confirming the findings of the SPOC pipeline. Taking the TLS orbital periods and transit times as our initial guesses, we performed a preliminary fit to the TESS light curve with allesfitter. For our final fit to the TESS data, we assumed circular orbits and fitted a transit model with nine free parameters:

1. the planet-to-star radius ratio, $R_p/R_\star$, with uniform priors from zero to 1;
2. the sum of the planetary and stellar radii over the semimajor axis, $(R_p + R_\star)/a$, with uniform priors from zero to 1;
3. the cosine of the orbital inclination, $\cos i$, with uniform priors from zero to 1;
4. the planetary orbital period, P, with uniform priors from -0.05 to $+0.05$ days around the initial TLS guess,
5. the initial transit time, T_0, with uniform priors from -0.05 to $+0.05$ days around the initial TLS guess;
6. a quadratic stellar limb-darkening function, sampled uniformly with the triangular sampling technique of Kipping (2013);
7. white-noise (jitter) scaling terms for the TESS light curve; and
8. two GP hyperparameters for the Matern-3/2 kernel: the characteristic amplitude $\ln \sigma$ and the timescale $\ln \rho$.

We used a Markov Chain Monte Carlo (MCMC) algorithm, implemented by the affine-invariant MCMC ensemble sampler emcee, to determine the posterior probability distributions of all model parameters. We initialized the MCMC with 200 walkers, each taking 40,000 steps, and performed a burn-in of 10,000 steps for each chain before calculating the final posterior distributions. The resulting phase-folded light curves are shown in Figure 2, together with the best transit model. The associated fit parameters and their 1σ uncertainties are listed in Table 4. Figure 6 shows the posteriors for these model parameters. To ensure MCMC convergence, we required that the autocorrelation time for each parameter be larger than 30 (Foreman-Mackey et al. 2013).

For each planet candidate, we also derived additional system parameters, including the planetary radius, semimajor axis, orbital inclination, and equilibrium temperature; the stellar density; the ratio of the stellar radius to the planet's semimajor axis; and the light-curve observables imprinted by the planet, namely, the diluted transit depth, total transit duration, transit duration between ingress and egress, and impact parameter (see Table 4).

6. Discussion

6.1. Dynamical Analysis

6.1.1. Orbital Stability

An important test of orbital architectures derived from observation includes an analysis of the long-term dynamical stability. Such tests have been performed for numerous systems to investigate the validity of Keplerian solutions and the dynamical evolution of the systems (e.g., Fabrycky et al. 2014). For the HD 191939 system, we performed *N*-body integrations using the Mercury Integrator Package (Chambers 1999). Based on the stellar parameters shown in Table 3 and the orbital properties listed in Table 4, we constructed a dynamical simulation that spanned 10^7 simulation years. The starting eccentricity for the planets was fixed to that of circular orbits using the estimated planetary masses from Section 4.2.4. Since the innermost planet has a very short orbital period, we chose a conservative time step of 0.1 day to ensure accuracy of the dynamical model.

The results of the simulation indicate that the HD 191939 system is stable based on the observed orbital parameters. In addition, there is little interaction between the planets, and their eccentricities remain below 0.01 for the duration of the simulation, resulting in minimal impact on the insolation flux received by the planets that would affect climate (Kane & Torres 2017). In particular, the innermost planet retains a circular orbit, since it is the most massive and primarily influenced by the host star.

6.1.2. Potential for Additional Planets

In Section 5, we conducted a full TLS search for a 3σ detection of a fourth planet and found no evidence of it. To probe our sensitivity limit and investigate the detectability of planets that might still be hidden in the TESS data due to low S/N or data gaps, we also performed a series of injection recovery tests. In particular, we generated planet signals and injected them into the TESS light curves using allesfitter, with planet sizes ranging from 0.8 to 4 $R_\oplus$ and periods ranging from 2 to 160 days. We then searched for these signals with TLS and recorded a signal to be recovered if the detected period matched any multiple of half the injected period to better than 5%. We find that TESS's recovery is nearly complete for sub-Neptunes and super-Earths on orbits less than ~80 days (Figure 7). However, the regimes of Earth-sized planets and small exoplanets on longer orbits remain open for exploration. This means that more transiting planets amenable to atmospheric characterization might still await discovery in future TESS sectors, while RV and TTV monitoring might unveil additional nontransiting companions.

6.1.3. TTVs

The TTVs in multiplanetary systems are caused by deviations from Keplerian orbits due to gravitational interactions between the planets (e.g., Agol et al. 2005; Holman & Murray 2005; Lithwick et al. 2012; Agol & Fabrycky 2018). These interactions can be used to verify the planetary nature of a transit signal and characterize the planetary masses and the system's orbital architecture. The TTVs occur for systems in which pairs of planets orbit near mean-motion resonances (MMRs), where a "first-order MMR" is defined as the period ratio being close to $P_{in}/P_{out} \approx (i-1)/i$, whereby P_{in} and P_{out} are the periods of the inner and outer planets, and i is an integer. The planets' mid-transit times then show sinusoidal variations with the "TTV superperiod," $P_{TTV} = |i/P_{out} - (i-1)/P_{in}|^{-1}$.

For HD 191939, planets c and d are close to a first-order MMR with a period ratio near 3:4. We would thus expect a TTV superperiod of $P_{TTV} \sim 1500$ days—a factor of 10 longer

[44] The TLS searches for transit-like events in photometric light curves by fitting a physical transit model with ingress, egress, and stellar limb darkening. This method enhances the detection efficiency by ~10% relative to the standard box least-squares algorithm (Kovács et al. 2002), which fits a boxcar function to the transit signatures.

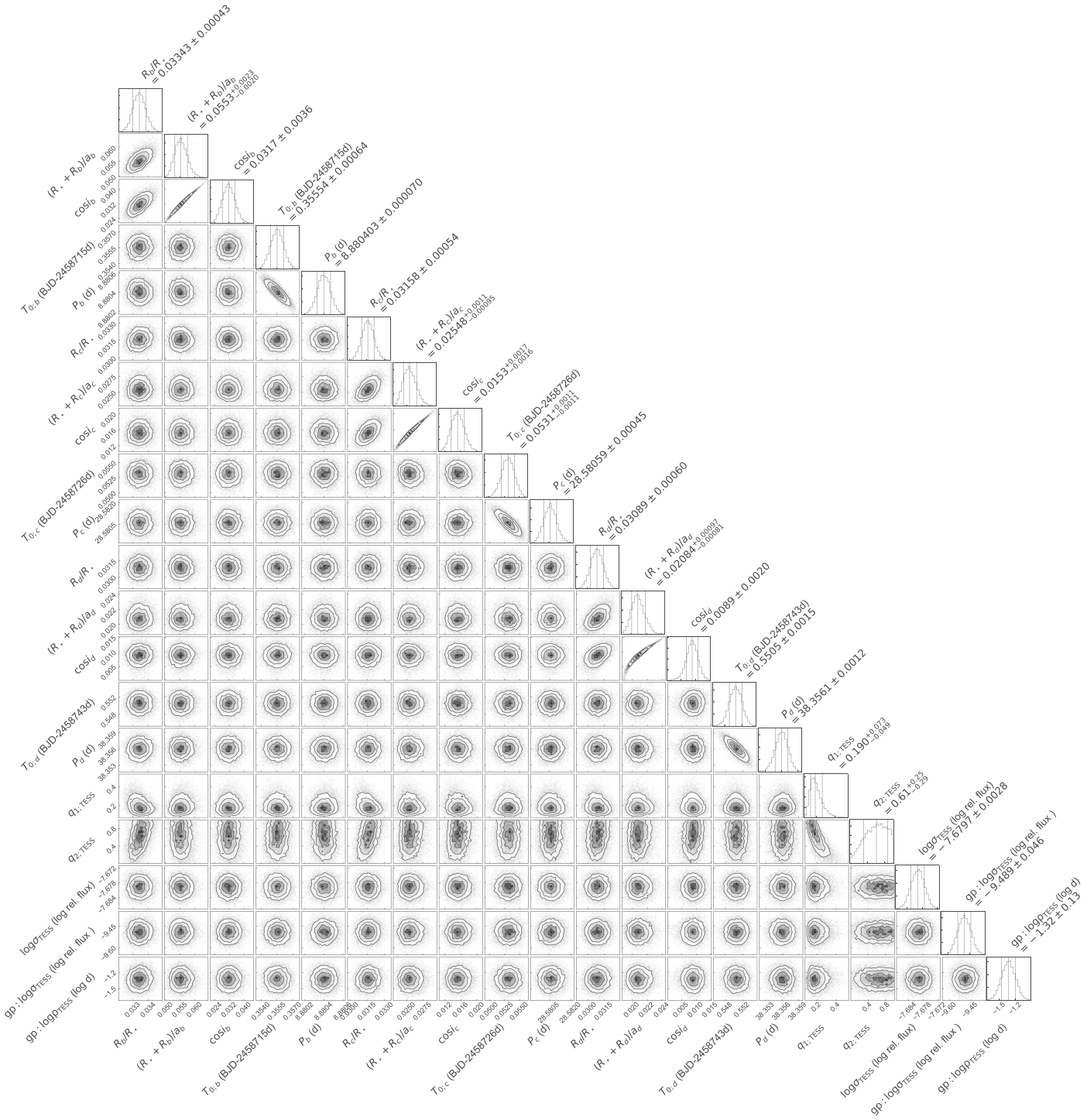

Figure 6. Posterior probability distributions for the `allesfitter` model parameters. The dashed lines show the 16th, 50th, and 84th percentiles.

than the span of our discovery data set (∼150 days). This means we are currently only starting to sample the TTVs of this system and are still in a regime where the linear period fits for planets c and d are likely biased. In contrast, the inner pair of planets, b and c, lie further off a second-order MMR with a period ratio near 1:3 and are thus expected to show much lower TTV amplitudes. In addition, short-timescale "chopping" variations can occur when the planets are closest to another on their orbits (e.g., Deck & Agol 2015). These chopping TTVs typically occur on harmonics of the synodic timescale, $P_{\mathrm{TTV;chopping}} = |1/P_{\mathrm{out}} - 1/P_{\mathrm{in}}|^{-1}$. For planets c and d, we expect this to happen on timescales of ∼100 days, well within the available observation range.

We searched for evidence of TTVs by performing an `allesfitter` fit to the TESS light curve. For this analysis, we froze the initial epoch and orbital period and fitted the rest of the transit parameters described in Section 5, with the addition of a TTV parameter for each transit to allow for a shift in the mid-transit time. For independent confirmation, we also used the `exoplanet` (Foreman-Mackey et al. 2019) software and

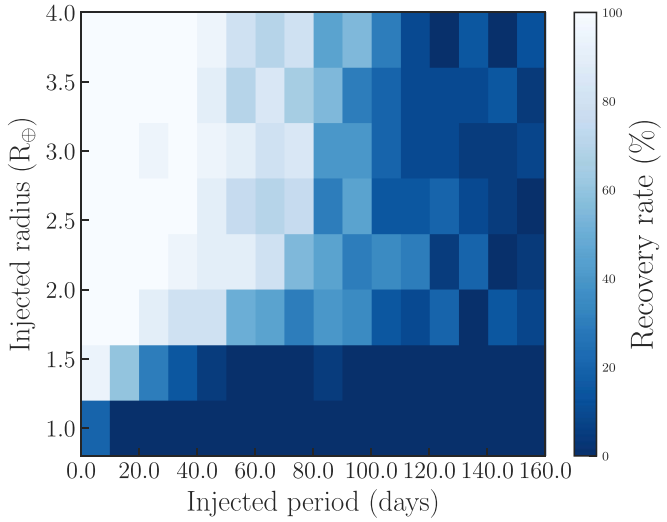

Figure 7. Injection recovery test for simulated transits of small planets (0.8–4 $R_\oplus$; y-axis) on periods between 2 and 160 days (x-axis). The color-coding shows the completeness of the recovery, with darker tones representing lower recovery rates. The TESS data for HD 191939 collected so far are near-complete for sub-Neptunes and super-Earths on orbits less than ∼80 days, but the regime of the smallest- and longest-period planets remains to be explored.

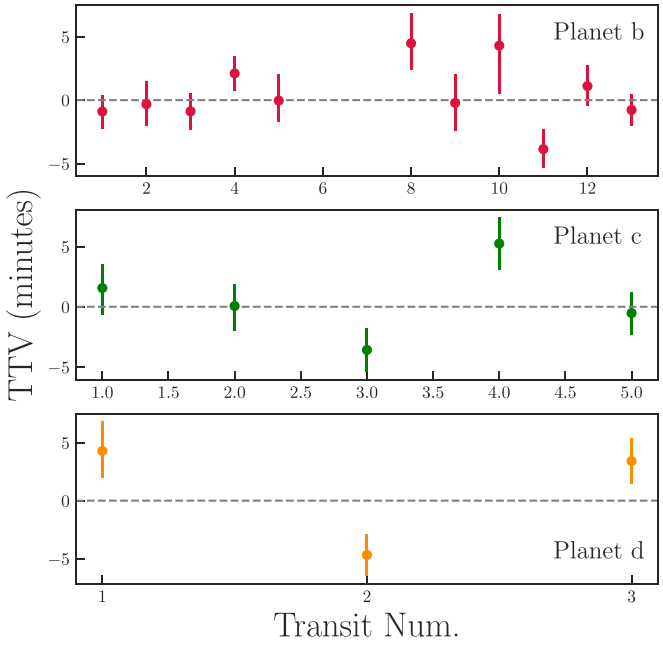

Figure 8. Search for TTV signals in the TESS data. From a free transit mid-time fit, we find per-transit deviations from linear ephemerides at ∼2σ, most notably for planets c and d. This could indicate a short-term TTV chopping signal.

modeled the planetary orbits using the `TTVOrbit` class with Gaussian priors on the system parameters (from Section 5, Table 4). In each study, we placed uniform priors on the mid-transit time of each observed transit in the TESS light curve, centered on the expected mid-transit time from the global fit (Table 4) with a width of 1 hr. We determined convergence once the fits reached a chain length of at least 30 times the autocorrelation length for `allesfitter` and a Gelman–Rubin statistic $\hat{R} < 1.001$ for `exoplanet` (Gelman & Rubin 1992).

While we find no significant evidence for the long-term superperiod TTVs (as expected), we recognize a deviation of the transit mid-times from strictly linear ephemerides on shorter timescales (Figure 8). This could either be due to noise or hint toward a chopping signal. Most notably, the first transit of planet d arrives 4.3 ± 2.5 minutes late, the second arrives 4.7 ± 1.8 minutes early, and the third arrives 3.4 ± 1.9 minutes late again. Similarly, the third transit of planet c arrives 3.6 ± 1.8 minutes early, and the fourth transit arrives 5.2 ± 2.1 minutes late. Future TESS observations and ground-based photometric follow-up will be needed to search for the first conclusive evidence of a chopping signal and constrain the presence of long-term superperiod TTV trends. Initial analyses could be possible after the first full year of monitoring with TESS, when a quarter of the superperiod will have been sampled.

6.2. Atmospheric Characterization Prospects

All three HD 191939 planets have the potential to be excellent transmission spectroscopy targets, contingent upon mass measurements. The equilibrium temperatures for a zero Bond albedo and efficient redistribution of heat to the nightside hemisphere are about 800, 550, and 500 K for planets b, c, and d, respectively. To estimate the amplitude of the atmospheres' transmission signal, we assumed hydrogen-dominated compositions and used the predicted masses from the probabilistic MR relation of Wolfgang et al. (2016; $M_b = 14.77^{+1.98}_{-1.97}$, $M_c = 13.85^{+1.87}_{-1.85}$, and $M_d = 13.50^{+1.84}_{-1.80}$ $M_\oplus$). Under these conditions, a change in the planet radius corresponding to one pressure scale height (H) would result in a change in the transit depth of ∼15 ppm for HD 191939 b and ∼10 ppm for both HD 191939 c and HD 191939 d. At near-infrared wavelengths, absorption due to species such as H_2O and CH_4 can produce variations of a few pressure scale heights in the effective planetary radius, translating to transmission signals $\gtrsim$10–80 ppm for all three planets. Given the brightness of the host star, this would put all three HD 191939 planets among the most favorable sub-Neptunes currently known for transmission spectroscopy.

To put HD 191939 in the broader context of confirmed sub-Neptunes suitable for atmospheric characterization, we downloaded a list from the NASA Exoplanet Archive of all confirmed planets with radii between 2 and 4 $R_\oplus$. We also required these planets to have mass measurements and a relative error in planet mass, planet radius, and host star radius less than 30%. For planets with multiple measurements of a given parameter, we selected the reported value with the lowest total uncertainty. We then calculated the expected S/N of each planet for a single transit as (Vanderburg et al. 2016)

$$\mathrm{S/N} \propto \frac{R_p H \sqrt{F t_{14}}}{R_*^2}, \tag{3}$$

with the atmosphere's scale height given by $H = \frac{k_b T_{eq}}{\mu g}$. Above, F is the stellar flux, k_b is Boltzmann's constant, T_{eq} is the planet's equilibrium temperature, μ is the atmospheric mean molecular weight, g is the planet's surface gravity, and t_{14} is the transit duration (Seager 2010). We computed the stellar flux from the host star's H-band 2MASS magnitude and set $\mu = 4$ amu, corresponding to approximately 100 times solar metallicity, in line with sub-Neptune formation simulations (Fortney et al. 2013). In the absence of the t_{14} and T_{eq} values listed in the

Table 5

Top Panel: Best Confirmed Sub-Neptunes ($R_p = 2 - 4R_\oplus$) for Transmission Spectroscopy. We Only Show Planets with Measured Masses and a Relative Error in Host Star Radius, Planet Radius, and Planet Mass Less Than 30%. Bottom Panel: Predicted S/N for the HD 191939 Planets

Planet Name	Host Star	J-magnitude (mag)	Relative S/N[b]	Planet Radius ($R_\oplus$)	Discovery	Planet Radius Reference
GJ 436 b	GJ 436	6.90	8.35 ± 0.14	$3.96^{+0.05}_{-0.05}$	W. M. Keck	Knutson et al. (2011)
GJ 1214 b	GJ 1214	9.75	7.69 ± 0.23	$2.74^{+0.06}_{-0.05}$	MEarth	Kundurthy et al. (2011)
π Men c	HD 39091	4.87	4.78 ± 0.28	$2.06^{+0.03}_{-0.03}$	TESS	Gandolfi et al. (2018)
HD 97658 b	HD 97658	6.20	2.34 ± 0.13	$2.247^{+0.098}_{-0.095}$	W. M. Keck	van Grootel et al. (2014)
HD 3167 c	HD 3167	7.55	1.63 ± 0.22	$2.85^{+0.24}_{-0.15}$	K2	Vanderburg et al. (2016)
GJ 9827 d	GJ 9827	7.98	1.45 ± 0.32	$2.022^{+0.046}_{-0.043}$	K2	Rice et al. (2019)
TOI-125 c	TOI-125	9.47	1.07 ± 0.25	$2.76^{+0.1}_{-0.1}$	TESS	Nielsen et al. (2020)
GJ 143 b	GJ 143	6.08	1.00 ± 0.18	$2.61^{+0.17}_{-0.16}$	TESS	Dragomir et al. (2019)
HD 15337 c	HD 15337	7.66	0.98 ± 0.30	$2.55^{+0.10}_{-0.10}$	TESS	Dumusque et al. (2019)
TOI-125 b	TOI-125	9.47	0.91 ± 0.18	$2.73^{+0.08}_{-0.08}$	TESS	Nielsen et al. (2020)
HD 191939 b[a]	HD 191939	7.59	1.81 ± 0.19	$3.42^{+0.11}_{-0.11}$	TESS	This work
HD 191939 c[a]	HD 191939	7.59	$1.33^{+0.19}_{-0.20}$	$3.23^{+0.11}_{-0.11}$	TESS	This work
HD 191939 d[a]	HD 191939	7.59	1.29 ± 0.20	$3.16^{+0.11}_{-0.11}$	TESS	This work

Notes. Data were retrieved from the NASA Exoplanet Archive in 2020 May.
[a] Planetary masses estimated from the MR relation of Wolfgang et al. (2016).
[b] The predicted S/N for all planets is given relative to that of GJ 143 b.

Exoplanet Archive, we computed these parameters with Equations (16) and (2.27) in Seager & Mallen-Ornelas (2003) and Seager (2010), respectively. For these calculations, we assumed a zero Bond albedo ($A_B = 0$) and full heat redistribution over the planet's surface ($f' = 1/4$).

Table 5 shows the HD 191939 planets and the best-known sub-Neptunes for atmospheric characterization work, according to Equation (3). Our study indicates that all three HD 191939 planets may be valuable candidates for transmission spectroscopy, with HD 191939 b offering the highest S/N predictions, followed by HD 191939 c and d. However, it is necessary to measure the planetary masses before this can be confirmed. Moreover, the relatively long periods of planets HD 191939 b and c (~29 and 38 days; see Table 4) may limit the number of transit events per observing campaign. This may make it more challenging to schedule and obtain the necessary observations to build up the required S/N for atmospheric characterization work, especially in comparison with the shorter-period planets in Table 5, such as GJ 436 b ($P \approx 2.6$ days) or GJ 1214 b ($P \approx 1.6$ days).

Figure 9 shows the HD 191939 planets in the context of the sub-Neptunes considered in this study. It also illustrates the planets' equilibrium temperatures and their transmission spectroscopy metric (TSM; Kempton et al. 2018).[45] From an anticipated S/N perspective, HD 3167c (Vanderburg et al. 2016) offers a useful point of comparison. The latter is a 2.9 $R_\oplus$ planet orbiting a bright ($J = 7.5$ mag) K0 V host star with a period of about 30 days, an equilibrium temperature of 600 K, and a transmission signal amplitude of ~20 ppm for a 1H change in effective planet radius. Given the similar brightness of the HD 3167 and HD 191939 host stars, this means that HD 191939 c and d could be comparably suited for transmission spectroscopy and that HD 191939 b could be more favorable than HD 3167 c owing to its higher equilibrium temperature and thus larger atmospheric scale height.

[45] The TSM predicts the expected transmission spectroscopy S/N of a 10 hr observing campaign with JWST/NIRISS under the assumption of a fixed MR relationship, cloud-free atmospheres, and the same atmospheric composition for all planets of a given type.

6.3. HD 191939 in Context

The Sun-like star HD 191939 hosts three transiting sub-Neptunes in a compact orbital configuration. This system is a promising candidate for detailed characterization, as evidenced by Figures 1 and 10.

First, the host star's brightness and proximity make HD 191939 an excellent target for future photometric follow-up. In the context of single- and multiplanet systems for which mass measurements are available and the relative error in host star radius, planet mass, and planet radius is less than 30% (see Figure 1), HD 191939 is one of the brightest and closest multis known to date. This also holds true when comparing HD 191939 to nearby ($d \leqslant 100$ pc) multiplanetary systems with Sun-like (FGK) stellar hosts (see Table 6).

A closer look at the properties of the systems listed in Table 6 reveals several interesting connections between HD 191939 and GJ 9827 (Niraula et al. 2017). The latter is composed of two planets in the super-Earth regime (GJ 9827 b and c) and an outer mini-Neptune (GJ 9827 d). Similar to HD 191939, GJ 9827 is a triplet in which all three planets transit their bright parent star. Both systems are near MMRs, with the former presenting a possible first- and second-order MMR (see Section 6.1.3) and the latter featuring period ratios near commensurability of 1:3:5. Finally, both HD 191939 and GJ 9827 exhibit similar S/N predictions for transmission spectroscopy (see Table 5). More specifically, GJ 9827 offers favorable prospects for the atmospheric characterization of its outer sub-Neptune. In the case of HD 191939, all three sub-Neptunes may be suitable for transmission spectroscopy. Such a study would offer the opportunity to perform a comparative study of the planets' atmospheres and investigate the fundamental properties of multiple sub-Neptunes born with a similar formation and evolutionary history.

In addition, HD 191939 is a valuable target for follow-up photometry due to its location in the northern ecliptic

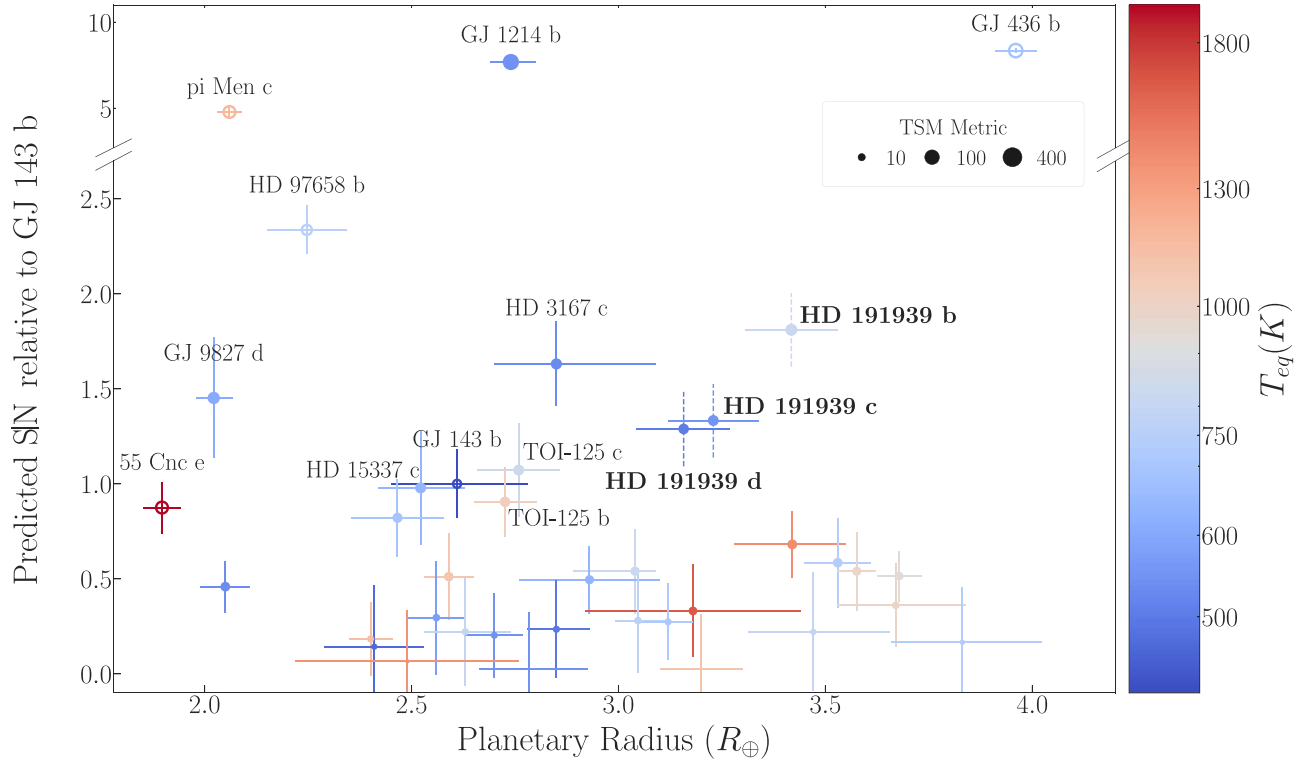

Figure 9. Predicted S/N relative to GJ 143 b for the population of confirmed sub-Neptunes (R_p = 2–4 $R_\oplus$), with the addition of 55 Cnc e ($R_p = 1.897^{+0.044}_{-0.046}$ $R_\oplus$; Dai et al. 2019) for comparison. We only present systems with mass measurements and a relative error in host star radius, planet radius, and planet mass less than 30%. The color of the marker represents the planet's equilibrium temperature, while its size indicates its TSM. Open circles are used for planets with a host star brighter than the JWST brightness limit ($J \approx 7$ mag; Beichman et al. 2014). Names are only displayed for the top 10 planets (see Table 5). We show the *y*-error bars of the HD 191939 planets with dashed lines to indicate that the S/N of the HD 191939 planets is based on mass estimates. Data were retrieved from the NASA Exoplanet Archive in 2020 May.

Table 6
HD 191939 Relative to Confirmed Multiplanetary Systems with FGK Stellar Hosts Located at a Distance of Less than 100 pc (Sorted by *K* Magnitude)

Host Name	K_s Magnitude (mag)	Distance (pc)	Spectral Type	Known Planets (No.)
HD 219134	3.26	6.53	K3 V	6
55 Cnc	4.02	12.59	G8 V	5
HD 39091	4.24	18.27	G0 V	2
GJ 143	5.38	16.32	K4.5	2
HD 213885	6.42	48.09	G	2
HAT-P-11	7.01	37.76	K4	2
HD 15337	7.04	44.81	K1 V	2
HD 3167	7.07	47.29	K0 V	3
HD 191939	7.18	53.48	G8 V	3
GJ 9827	7.19	29.66	K5 V	3
WASP-8	8.09	89.96	G8 V	2
TOI-1130	8.35	58.26	K	2
Kepler-93	8.37	95.91	G5	2
K2-141	8.40	61.87	K7 V	2
HAT-P-17	8.54	92.38	K	2

Note. Data were retrieved from the NASA Exoplanet Archive in 2020 May.

hemisphere sky. Indeed, HD 191939 lies in a region where 10 TESS sectors overlap (sectors 14–19, 21–22, and 24–25), hence enabling a long TESS observational baseline. In particular, HD 191939 will have been monitored for about 10 months once TESS sector 25 (2020 June 8) concludes and will be reobserved for an additional ∼10 months during the TESS extended mission. As a result, HD 191939 will have a photometric baseline of almost ∼3 yr. Such a long time span will facilitate a variety of dynamical studies, including a refinement of the system's transit ephemerides and a search for additional planetary companions via TTV analyses. Moreover, the proximity of the host star (∼54 pc) will also facilitate searches for massive planetary companions on wide orbits (∼1 au) using Gaia astrometry (Perryman et al. 2014).

From the perspective of ground-based RV follow-up, HD 191939 is also an excellent target for future observations due to its brightness, slow rotation, and lack of measurable chromospheric activity. Future RV monitoring with spectrographs such as CARMENES (Quirrenbach et al. 2014, 2018) or HARPS (Cosentino et al. 2012) will soon enable precise measurements of the planets' masses. An RV monitoring campaign carried out by the CARMENES consortium is currently ongoing to confirm and further characterize the HD 191939 planets. Due to the system's complex orbital architecture, however, a large number of measurements will be needed to accurately constrain the physical properties of the system.

With three temperate sub-Neptunes, HD 191939 may also be a prime system for atmospheric studies with present (e.g., the Hubble Space Telescope) and future (e.g., JWST, Extremely Large Telescope) facilities. With a high S/N for multi-wavelength transmission spectroscopy (see Table 5), the three HD 191939 planets appear to be among the best candidates for atmospheric characterization work (Figure 9). Their final suitability will be confirmed when mass measurements become

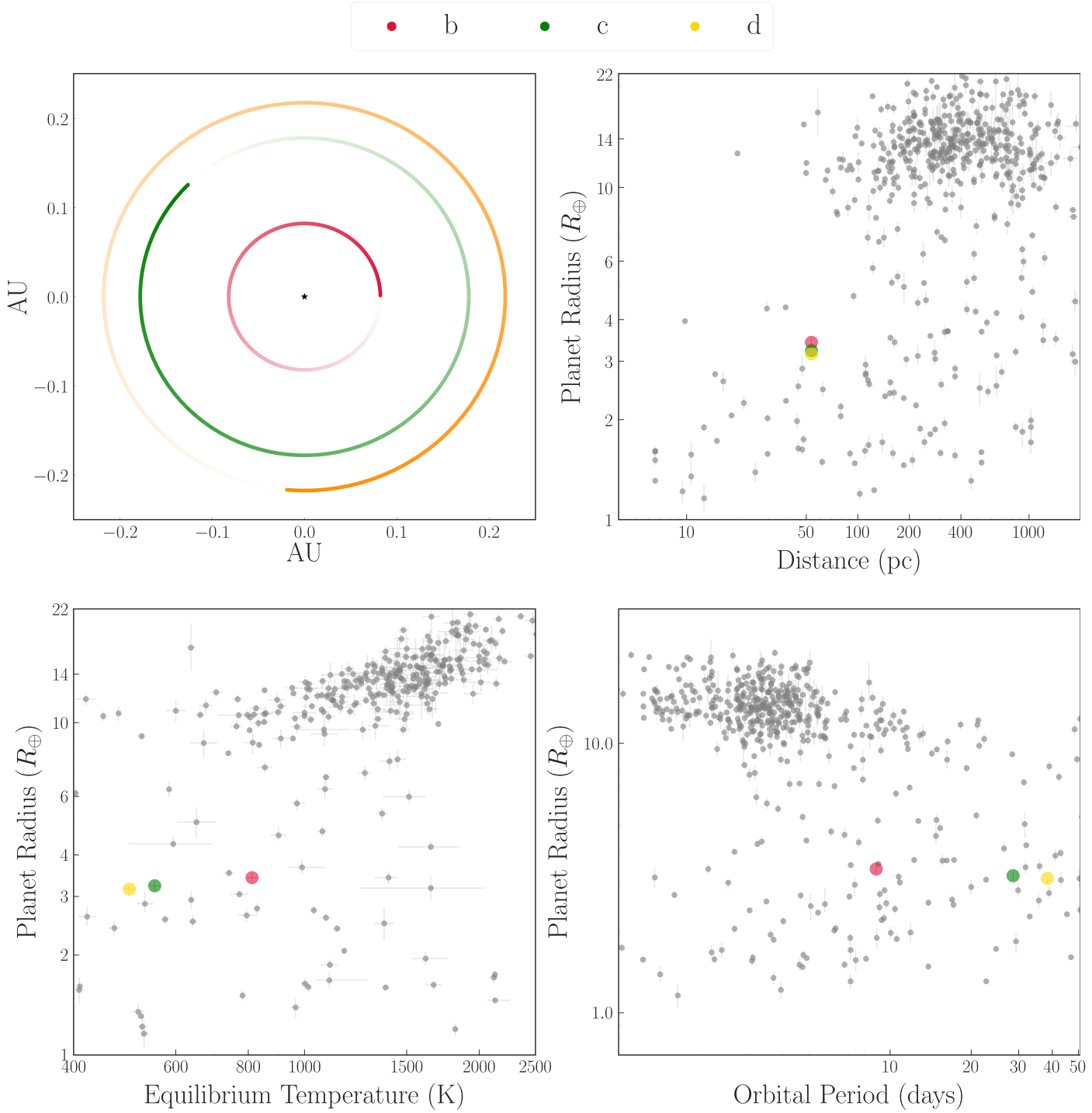

Figure 10. Planets b, c, and d are shown in red, green, and orange, respectively. Top left: top-down view of the HD 191939 system, with the sizes of the planets drawn to scale. Top right, bottom left, and bottom right: planet radius as a function of distance, equilibrium temperature, and orbital period, respectively. The systems shown in these views have mass measurements for at least one of their planets and a relative error in host star radius, planet radius, and planet mass better than 30%. Data were retrieved from the NASA Exoplanet Archive in 2020 May.

available. With regard to JWST in particular, HD 191939 will be visible for more than 200 days yr^{-1} due to its high ecliptic latitude (see Table 1).[46] Future observations will provide an opportunity to study the atmospheres, interiors, and habitability conditions of the HD 191939 planets.

Finally, the multiplanetary nature of HD 191939 provides a fantastic opportunity to perform comparative exoplanetology. By studying the physical and orbital characteristics of HD 191939 and comparing them to the properties of the known population of multitransiting planetary systems, we may gain insight into the distribution and occurrence rates of planets across a wide range of masses and radii, as well as the formation and evolution of planetary architectures.

[46] https://jwst-docs.stsci.edu/jwst-observatory-hardware/jwst-target-viewing-constraints

7. Conclusion

We have presented the TESS discovery of three sub-Neptune-sized planets around the nearby, bright Sun-like star HD 191939. We have confirmed the planetary nature of each planet candidate, both empirically through optical, photometric, and spectroscopic observations and statistically via the public FPP implementation `vespa`. Upon refining the stellar parameters of HD 191939 reported by TICv8, we have derived the physical and orbital properties of the system with an `allesfitter` fit to the TESS discovery light curve. In addition, we have conducted a dynamical study of the HD 191939 planets that indicates that they are in a compact and stable orbital configuration consistent with circular orbits. Finally, we have demonstrated that the system is a promising target for precise photometric and RV follow-up, as well as future atmospheric characterization studies.

Funding for this research is provided by the Massachusetts Institute of Technology, the MIT Torres Fellow Program, and the MIT Kavli Institute. We acknowledge the use of public TESS Alert data from pipelines at the TESS Science Office and the TESS Science Processing Operations Center. Funding for the TESS mission is provided by NASA's Science Mission directorate. This research has made use of the Exoplanet Follow-up Observation Program website, which is operated by the California Institute of Technology, under contract with the National Aeronautics and Space Administration under the Exoplanet Exploration Program. Resources supporting this work were provided by the NASA High-End Computing (HEC) Program through the NASA Advanced Supercomputing (NAS) Division at Ames Research Center for the production of the SPOC data products. This paper includes data collected by the TESS mission that are publicly available from the Mikulski Archive for Space Telescopes (MAST). The STScI is operated by the Association of Universities for Research in Astronomy, Inc., under NASA contract NAS 5-26555. This research has made use of the NASA Exoplanet Archive, which is operated by the California Institute of Technology, under contract with the National Aeronautics and Space Administration under the Exoplanet Exploration Program. The Digitized Sky Surveys were produced at the Space Telescope Science Institute under U.S. Government grant NAG W-2166. The images of these surveys are based on photographic data obtained using the Oschin Schmidt Telescope on Palomar Mountain and the UK Schmidt Telescope. The plates were processed into the present compressed digital form with the permission of these institutions. The National Geographic Society—Palomar Observatory Sky Atlas (POSS-I) was made by the California Institute of Technology with grants from the National Geographic Society. The Second Palomar Observatory Sky Survey (POSS-II) was made by the California Institute of Technology with funds from the National Science Foundation, the National Geographic Society, the Sloan Foundation, the Samuel Oschin Foundation, and the Eastman Kodak Corporation. This work has made use of data from the European Space Agency (ESA) mission Gaia (https://www.cosmos.esa.int/gaia), processed by the Gaia Data Processing and Analysis Consortium (DPAC; https://www.cosmos.esa.int/web/gaia/dpac/consortium). Funding for the DPAC has been provided by national institutions, in particular the institutions participating in the Gaia Multilateral Agreement. This paper used data retrieved from the SOPHIE archive at Observatoire de Haute-Provence (OHP), available at atlas.obs-hp.fr/sophie. The AO images presented in this paper were obtained at the Gemini Observatory (Program ID: GN-2019B-LP-101), which is operated by the Association of Universities for Research in Astronomy, Inc., under a cooperative agreement with the NSF on behalf of the Gemini partnership: the National Science Foundation (United States), National Research Council (Canada), CONICYT (Chile), Ministerio de Ciencia, Tecnología e Innovación Productiva (Argentina), Ministério da Ciência, Tecnologia e Inovação (Brazil), and Korea Astronomy and Space Science Institute (Republic of Korea).

The authors thank Amanda Bosh (MIT), Tim Brothers (MIT Wallace Astrophysical Observatory), Julien de Wit (MIT), Artem Burdanov (MIT), Songhu Wang (Yale University), Enrique Herrero (IEEC/OAdM), Jonathan Irwin (Harvard-CfA), Samuel Hadden (Harvard-CfA), Özgür Başẗurk (Ankara University), Ergün Ege (Istanbul University), and Brice-Olivier Demory (University of Bern) for helping to coordinate follow-up observations.

We thank the anonymous referee for helpful comments and suggestions that greatly improved this work. M.N.G. and C.X.H. acknowledge support from MIT's Kavli Institute as Juan Carlos Torres Fellows. T.D. acknowledges support from MIT's Kavli Institute as a Kavli postdoctoral fellow. A.V.'s work was performed under contract with the California Institute of Technology/Jet Propulsion Laboratory, funded by NASA through the Sagan Fellowship Program executed by the NASA Exoplanet Science Institute. I.R. acknowledges support from the Spanish Ministry of Science, Innovation and Universities (MCIU) and the Fondo Europeo de Desarrollo Regional (FEDER) through grant PGC2018-098153-B-C33, as well as the support of the Generalitat de Catalunya/CERCA program. B.V.R. and J.N.W. thank the Heising-Simons Foundation for support. I.J.M.C. acknowledges support from the NSF through grant AST-1824644 and NASA through Caltech/JPL grant RSA-1610091.

Facilities: TESS, FLWO: 1.5 m (TRES), LCO: 1 m (NRES), OHP: 1.93 m (SOPHIE), Gemini/NIRI, OAA: 0.4 m.

Software: `Python` (van Rossum 1995), `numpy` (Oliphant 2006), `scipy` (Virtanen et al. 2020), `matplotlib` (Hunter 2007), `astropy` (Price-Whelan et al. 2018), `pandas` (McKinney 2010), `allesfitter` (Günther & Daylan 2020, and in preparation) `emcee` (Foreman-Mackey et al. 2013), `corner` (Foreman-Mackey 2016), `tqdm` (da Costa-Luis et al. 2020), `lightkurve` (Lightkurve Collaboration et al. 2018), `Transit Least Squares` (Hippke & Heller 2019), `vespa` (Morton 2012), `isochrones` (Morton 2015), `isoclassify` (Huber et al. 2017), `forecaster` (Chen & Kipping 2017), `exoplanet` (Foreman-Mackey et al. 2019), `starry` (Luger et al. 2019), `pymc3` (Salvatier et al. 2016), `theano` (Theano Development Team et al. 2016), `rebound` (Rein & Liu 2012).

ORCID iDs

Mariona Badenas-Agusti https://orcid.org/0000-0003-4903-567X
Maximilian N. Günther https://orcid.org/0000-0002-3164-9086
Tansu Daylan https://orcid.org/0000-0002-6939-9211
Thomas Mikal-Evans https://orcid.org/0000-0001-5442-1300
Andrew Vanderburg https://orcid.org/0000-0001-7246-5438
Chelsea X. Huang https://orcid.org/0000-0003-0918-7484
Elisabeth Matthews https://orcid.org/0000-0003-0593-1560
Benjamin V. Rackham https://orcid.org/0000-0002-3627-1676
Allyson Bieryla https://orcid.org/0000-0001-6637-5401
Keivan G. Stassun https://orcid.org/0000-0002-3481-9052
Stephen R. Kane https://orcid.org/0000-0002-7084-0529
Avi Shporer https://orcid.org/0000-0002-1836-3120

Benjamin J. Fulton https://orcid.org/0000-0003-3504-5316
Michelle L. Hill https://orcid.org/0000-0002-0139-4756
Grzegorz Nowak https://orcid.org/0000-0002-7031-7754
Ignasi Ribas https://orcid.org/0000-0002-6689-0312
Enric Pallé https://orcid.org/0000-0003-0987-1593
Jon M. Jenkins https://orcid.org/0000-0002-4715-9460
David W. Latham https://orcid.org/0000-0001-9911-7388
Sara Seager https://orcid.org/0000-0002-6892-6948
George R. Ricker https://orcid.org/0000-0003-2058-6662
Roland K. Vanderspek https://orcid.org/0000-0001-6763-6562
Joshua N. Winn https://orcid.org/0000-0002-4265-047X
Oriol Abril-Pla https://orcid.org/0000-0002-1847-9481
Karen A. Collins https://orcid.org/0000-0001-6588-9574
Pere Guerra Serra https://orcid.org/0000-0002-4308-2339
Prajwal Niraula https://orcid.org/0000-0002-8052-3893
Zafar Rustamkulov https://orcid.org/0000-0003-4408-0463
Thomas Barclay https://orcid.org/0000-0001-7139-2724
Steve B. Howell https://orcid.org/0000-0002-2532-2853
David R. Ciardi https://orcid.org/0000-0002-5741-3047
Joshua E. Schlieder https://orcid.org/0000-0001-5347-7062
Douglas A. Caldwell https://orcid.org/0000-0003-1963-9616
Michael Fausnaugh https://orcid.org/0000-0002-9113-7162
Martin Paegert https://orcid.org/0000-0001-8120-7457
Joshua Pepper https://orcid.org/0000-0002-3827-8417
Mark E. Rose https://orcid.org/0000-0003-4724-745X
Joseph D. Twicken https://orcid.org/0000-0002-6778-7552

References

Agol, E., & Fabrycky, D. C. 2018, in Handbook of Exoplanets, ed. H. Deeg & J. Belmonte (Cham: Springer), 7
Agol, E., Steffen, J., Sari, R., & Clarkson, W. 2005, MNRAS, 359, 567
Baranne, A., Queloz, D., Mayor, M., et al. 1996, A&AS, 119, 373
Beichman, C., Benneke, B., Knutson, H., et al. 2014, arXiv:1411.1754
Bouchy, F., Hébrard, G., Delfosse, X., et al. 2011, in EPSC-DPS Joint Meeting 2011 (Göttingen: Copernicus Gesellschaft mbH), 240
Bouchy, F., Hébrard, G., Udry, S., et al. 2009, A&A, 505, 853
Brandeker, A., & Cataldi, G. 2019, A&A, 621, A86
Bressan, A., Marigo, P., Girardi, L., et al. 2012, MNRAS, 427, 127
Brown, A. G. A., Vallenari, A., Prusti, T., et al. 2018, A&A, 616, A1
Brown, T. M., Baliber, N., Bianco, F. B., et al. 2013, PASP, 125, 1031
Buchhave, L. A., Bakos, G. Á, Hartman, J. D., et al. 2010, ApJ, 720, 1118
Buchhave, L. A., Latham, D. W., Johansen, A., et al. 2012, Natur, 486, 375
Cannon, A. J., & Pickering, E. C. 1993, yCat, 3135, 0
Chambers, J. E. 1999, MNRAS, 304, 793
Chen, J., & Kipping, D. 2017, ApJ, 834, 17
Choi, J., Dotter, A., Conroy, C., et al. 2016, ApJ, 823, 102
Ciardi, D. R., Beichman, C. A., Horch, E. P., & Howell, S. B. 2015, ApJ, 805, 16
Claret, A., & Bloemen, S. 2011, A&A, 529, A75
Cloutier, R., Doyon, R., Bouchy, F., & Hébrard, G. 2018, AJ, 156, 82
Coelho, P., Barbuy, B., Meléndez, J., Schiavon, R. P., & Castilho, B. V. 2005, A&A, 443, 735
Collins, K. A., Kielkopf, J. F., Stassun, K. G., & Hessman, F. V. 2017, AJ, 153, 77
Coroller, H. L., & Bouchy, F. 2017, SOPHIE: Documentation Pour Les Utilisateurs, Version 4.0, http://www.obs-hp.fr/guide/sophie/docs/Doc_SOPHIE_v4.pdf
Cosentino, R., Lovis, C., Pepe, F., et al. 2012, Proc. SPIE, 8446, 84461V
Cutri, R. M., Skrutskie, M. F., van Dyk, S., et al. 2003, yCat, 2246, 0
da Costa-Luis, C., Larroque, S. K., Altendorf, K., et al. 2020, tqdm: A fast, Extensible Progress Bar for Python and CLI (Version v4.47.0), Zenodo, doi:10.5281/zenodo.3912045
da Silva, L., Girardi, L., Pasquini, L., et al. 2006, A&A, 458, 609
Dai, F., Masuda, K., Winn, J. N., & Zeng, L. 2019, ApJ, 883, 79
Deck, K. M., & Agol, E. 2015, ApJ, 802, 116
Dotter, A. 2016, ApJS, 222, 8
Dragomir, D., Teske, J., Günther, M. N., et al. 2019, ApJL, 875, L7
Dumusque, X., Turner, O., Dorn, C., et al. 2019, A&A, 627, A43
Fabrycky, D. C., Lissauer, J. J., Ragozzine, D., et al. 2014, ApJ, 790, 146
Foreman-Mackey, D. 2016, JOSS, 1, 24
Foreman-Mackey, D., Czekala, I., Luger, R., et al. 2019, dfm/exoplanet v0.2.3, Zenodo, doi:10.5281/zenodo.1998447
Foreman-Mackey, D., Hogg, D. W., Lang, D., & Goodman, J. 2013, PASP, 125, 306
Fortney, J. J., Mordasini, C., Nettelmann, N., et al. 2013, ApJ, 775, 80
Fressin, F., Torres, G., Charbonneau, D., et al. 2013, ApJ, 766, 81
Fulton, B. J., & Petigura, E. A. 2018, AJ, 156, 264
Fürész, G. 2008, PhD thesis, Univ. Szeged
Gandolfi, D., Barragán, O., Livingston, J. H., et al. 2018, A&A, 619, L10
Gelman, A., & Rubin, D. B. 1992, StaSc, 7, 457
Green, G. M., Schlafly, E. F., Finkbeiner, D., et al. 2018, MNRAS, 478, 651
Guerrero, N. 2020, AAS Meeting, 235, 327.03
Günther, M. N., & Daylan, T. 2020, arXiv:2003.14371
Günther, M. N., Pozuelos, F. J., Dittmann, J. A., et al. 2019, NatAs, 3, 1099
Hippke, M., & Heller, R. 2019, A&A, 623, A39
Hodapp, K. W., Jensen, J. B., Irwin, E. M., et al. 2003, PASP, 115, 1388
Høg, E., Fabricius, C., Makarov, V. V., et al. 2000, A&A, 355, L27
Holman, M. J., & Murray, N. W. 2005, Sci, 307, 1288
Howard, A. W., Marcy, G. W., Johnson, J. A., et al. 2010, Sci, 330, 653
Huang, C. X., Burt, J., Vanderburg, A., et al. 2018, ApJL, 868, L39
Huber, D., Zinn, J., Bojsen-Hansen, M., et al. 2017, ApJ, 844, 102
Hunter, J. D. 2007, CSE, 9, 90
Jenkins, J. M. 2017, Kepler Data Processing Handbook, Kepler Science Document, KSCI-19081-002
Jenkins, J. M., Twicken, J. D., McCauliff, S., et al. 2016, Proc. SPIE, 9913, 99133E
Kaiser, N., Aussel, H., Burke, B. E., et al. 2002, Proc. SPIE, 4836, 154
Kaiser, N., Burgett, W., Chambers, K., et al. 2010, Proc. SPIE, 7733, 77330E
Kane, S. R., & Torres, S. M. 2017, AJ, 154, 204
Kempton, E. M.-R., Bean, J. L., Louie, D. R., et al. 2018, PASP, 130, 114401
Kipping, D. M. 2013, MNRAS, 435, 2152
Knutson, H. A., Madhusudhan, N., Cowan, N. B., et al. 2011, ApJ, 735, 27
Kovács, G., Zucker, S., & Mazeh, T. 2002, A&A, 391, 369
Kundurthy, P., Agol, E., Becker, A. C., et al. 2011, ApJ, 731, 123
Kurucz, R. L. 1992, in IAU Symp. 149, The Stellar Populations of Galaxies, ed. B. Barbuy & A. Renzini (Dordrecht: Kluwer), 225
Latham, D. W., Rowe, J. F., Quinn, S. N., et al. 2011, ApJL, 732, L24
Lightkurve Collaboration, Cardoso, J. V. d. M., Hedges, C., et al. 2018, Lightkurve: Kepler and TESS Time Series Analysis in Python, v 1.11, Astrophysics Source Code Library, ascl:1812.013
Lissauer, J. J., Marcy, G. W., Bryson, S. T., et al. 2014, ApJ, 784, 44
Lissauer, J. J., Marcy, G. W., Rowe, J. F., et al. 2012, ApJ, 750, 112
Lissauer, J. J., Ragozzine, D., Fabrycky, D. C., et al. 2011, ApJS, 197, 8
Lithwick, Y., Xie, J., & Wu, Y. 2012, ApJ, 761, 122
Lomb, N. R. 1976, Ap&SS, 39, 447
Lovis, C., & Fischer, D. 2010, in Exoplanets, ed. S. Seager (Tucson, AZ: Univ. Arizona Press), 27
Luger, R., Agol, E., Foreman-Mackey, D., et al. 2019, AJ, 157, 64
Mandel, K., & Agol, E. 2002, ApJL, 580, L171
McKinney, W. 2010, in Proc. 9th Python in Science Conf., ed. S. van der Walt & J. Millman (Austin, TX: SciPy), 51, https://conference.scipy.org/proceedings/scipy2010/pdfs/mckinney.pdf
Minkowski, R. L., & Abell, G. O. 1963, in Basic Astronomical Data: Stars and stellar systems, ed. K. A. Strand (Chicago, IL: Univ. Chicago Press), 481
Miralda-Escudé, J. 2002, ApJ, 564, 1019
Morton, T. D. 2012, ApJ, 761, 6
Morton, T. D. 2015, Isochrones: Stellar Model Grid Package, v 0.6, Astrophysics Source Code Library, ascl:1503.010
Moultaka, J., Ilovaisky, S., Prugniel, P., & Soubiran, C. 2004, in SF2A-2004: Semaine de l'Astrophysique Francaise, ed. F. Combes et al. (Les Ulis: EDP Sciences), 547
Nielsen, L. D., Gandolfi, D., Armstrong, D. J., et al. 2020, MNRAS, 492, 5399
Niraula, P., Redfield, S., Dai, F., et al. 2017, AJ, 154, 266
Oliphant, T. 2006, Guide to NumPy (2nd ed.; Scotts Valley, CA: CreateSpace)
Pecaut, M. J., & Mamajek, E. E. 2013, ApJS, 208, 9
Pecaut, M. J., Mamajek, E. E., & Bubar, E. J. 2012, ApJ, 746, 154
Perruchot, S., Kohler, D., Bouchy, F., et al. 2008, Proc. SPIE, 7014, 70140J
Perryman, M., Hartman, J., Bakos, G. Á, & Lindegren, L. 2014, ApJ, 797, 14
Petigura, E. A. 2005, PhD thesis, Univ. California
Petigura, E. A., Crossfield, I. J. M., Isaacson, H., et al. 2017, AJ, 155, 21
Press, W. H., Teukolsky, S. A., Vetterling, W. T., & Flannery, B. P. 1992, Numerical Recipes: The Art of Scientific Computing (Cambridge: Cambridge Univ. Press)
Price-Whelan, A. M., Sipőcz, B. M., Günther, H. M., et al. 2018, AJ, 156, 18

Quinn, S. N., Becker, J. C., Rodriguez, J. E., et al. 2019, AJ, 158, 177
Quirrenbach, A., Amado, P. J., Caballero, J. A., et al. 2014, Proc. SPIE, 9147, 91471F
Quirrenbach, A., Amado, P. J., Ribas, I., et al. 2018, Proc. SPIE, 10702, 107020W
Ragozzine, D., & Holman, M. J. 2010, arXiv:1006.3727
Reid, I. N., Brewer, C., Brucato, R. J., et al. 1991, PASP, 103, 661
Rein, H., & Liu, S. F. 2012, A&A, 537, A128
Rice, K., Malavolta, L., Mayo, A., et al. 2019, MNRAS, 484, 3731
Ricker, G. R., Winn, J. N., Vanderspek, R., et al. 2014, JATIS, 1, 014003
Rowe, J. F., Bryson, S. T., Marcy, G. W., et al. 2014, ApJ, 784, 45
Salvatier, J., Wiecki, T. V., & Fonnesbeck, C. 2016, PeerJ Computer Science, 2, e55
Scargle, J. D. 1982, ApJ, 263, 835
Schlegel, D. J., Finkbeiner, D. P., & Davis, M. 1998, ApJ, 500, 525
Seager, S. 2010, Exoplanet Atmospheres: Physical Processes (Princeton, NJ: Princeton Univ. Press)
Seager, S., & Mallen-Ornelas, G. 2003, ApJ, 585, 1038
Siverd, R. J., Brown, T. M., Barnes, S., et al. 2018, Proc. SPIE, 10702, 107026C
Siverd, R. J., Brown, T. M., Hygelund, J., et al. 2016, Proc. SPIE, 9908, 99086X
Spada, F., Demarque, P., Kim, Y. C., & Sills, A. 2013, ApJ, 776, 87
Stassun, K. G., Collins, K. A., & Gaudi, B. S. 2017, AJ, 153, 136
Stassun, K. G., Corsaro, E., Pepper, J. A., & Gaudi, B. S. 2018, AJ, 155, 22
Stassun, K. G., Oelkers, R. J., Pepper, J., et al. 2018, AJ, 156, 102
Stassun, K. G., & Torres, G. 2016, AJ, 152, 180
Stassun, K. G., & Torres, G. 2018, ApJ, 862, 61
Theano Development Team, Al-Rfou, R., Alain, G., et al. 2016, arXiv:1605.02688
Torres, G., Andersen, J., & Giménez, A. 2010, A&ARv, 18, 67
Twicken, J. D., Catanzarite, J. H., Clarke, B. D., et al. 2018, PASP, 130, 064502
van Grootel, V., Gillon, M., Valencia, D., et al. 2014, ApJ, 786, 2
van Leeuwen, F. 2007, A&A, 474, 653
van Rossum, G. 1995, Python tutorial, Technical Report CS-R9526, https://ir.cwi.nl/pub/5007/05007D.pdf
Vanderburg, A., Bieryla, A., Duev, D. A., et al. 2016, ApJ, 829, L9
Virtanen, P., Gommers, R., Oliphant, T. E., et al. 2020, NaMe, 17, 261
Wolfgang, A., Rogers, L. A., & Ford, E. B. 2016, ApJ, 825, 19
Yi, S., Demarque, P., Kim, Y.-C., et al. 2001, ApJS, 136, 417